



D/H of late Miocene meteoric waters in Western Australia: Paleoenvironmental conditions inferred from the δD of (U-Th)/He-dated CID goethite

Crayton J. Yapp^{a,*}, David L. Shuster^{b,c}

^a *Huffington Department of Earth Sciences, Southern Methodist University, Dallas, TX 75275-0395, United States*

^b *Department of Earth and Planetary Science, University of California, Berkeley, CA 94720, United States*

^c *Berkeley Geochronology Center, 2455 Ridge Road, Berkeley, CA 94709, United States*

Received 20 March 2017; accepted in revised form 21 June 2017; Available online 30 June 2017

Abstract

Nineteen (U-Th)/He ages were determined for eight samples from a core drilled in an ore-grade channel iron deposit (CID) of the Robe Pisolite (Robe Formation) of Mesa J in Western Australia. With one exception, uncorrected ages of the analyzed aliquots range from $6.7_{(\pm 0.4)}$ Ma to $30.2_{(\pm 3.1)}$ Ma, while molar ratios of Th/U range from 0.42 to 5.06. The exception is an aliquot with an apparent age of 2.7 Ma and Th/U of 5.70. A three-component mixing model involving one generation of goethite and two generations of hematite suggests that the age of crystallization of the oolitic goethites is $\sim 7_{(\pm 1)}$ Ma. If so, the goethites have effectively been closed systems for ~ 7 million years and should preserve a stable hydrogen isotope record of late Miocene rainfall in the vicinity of Mesa J. Cenozoic movement of the Australian continent had placed Mesa J and environs in the subtropics at a paleolatitude of about 29°S during the late Miocene.

Al-adjusted δD values of oolitic goethite in the eight CID samples range from -153‰ to -146‰ and imply that the δD of the late Miocene meteoric waters ranged from -61‰ to -53‰ , with an average of -56‰ . These relatively negative δD values might indicate that near-coastal, late Miocene rain was derived primarily from summer-season tropical cyclones with storm tracks that extended into the subtropics of western Australia. The postulated late Miocene tropical cyclones would have occurred more often and/or exhibited greater intensity at a paleolatitude of 29°S than is the case for modern sites at approximately 30°S on the west coast of Australia (e.g., Perth).

Higher fluxes of meteoric water in the Miocene summers would have facilitated dissolution and removal of BIF-sourced silica with concomitant enrichment in oxidized Fe. Moreover, wetter late Miocene summers could have promoted multiple cycles of microbially mediated dissolution and recrystallization of Fe(III) oxides in the aerobic systems. The oolitic textures may be indicative of such recycling. However, the oolitic goethites of Mesa J were closed systems after ~ 7 Ma. Therefore, the climate in the vicinity of Mesa J seems to have changed in the late Miocene to conditions that did *not* favor widespread recycling of Fe (III) oxides—perhaps changing from seasonally wet to the modern dry climate.

© 2017 Elsevier Ltd. All rights reserved.

Keywords: Hydrogen isotopes; Goethite; Miocene; CID; Meteoric water; Tropical cyclones; (U-Th)/He ages

1. INTRODUCTION

The Fe (III) oxides, goethite ($\alpha\text{-FeOOH}$) and hematite ($\alpha\text{-Fe}_2\text{O}_3$), are widespread products of oxidative chemical weathering in Earth's surface and near-surface environ-

* Corresponding author.

E-mail address: cjyapp@smu.edu (C.J. Yapp).

ments (Garrels and Christ, 1965) and can occur in comparatively high concentrations in ferricretes, laterites, and oolitic ironstones that formed at various times throughout the Phanerozoic (e.g., Van Houten, 1982; Van Houten and Bhattacharyya, 1982; Siehl and Thein, 1989; Young and Taylor, 1989). In some instances, such systems have been exploited as iron ores (e.g., Maynard, 1983).

Goethite/hematite-rich ooids and pisoids in the channel iron deposits (CID) of Western Australia are especially noteworthy examples of ore-grade accumulations of Fe (III) oxides and appear to be relics of pedogenic processes (Morris and Ramanaidou, 2007). Textural evidence linking lateritic weathering to the formation of ferruginous ooids in West African soils lends some support to the idea of a pedogenic origin for the ooids in the CID (Nahon et al., 1980). In addition to the ooids, there are ferruginized detrital wood fragments and, in the pores of the CID, some post-aggradation, diagenetic goethite (Morris and Ramanaidou, 2007; Danišik et al., 2013).

The ooids/pisoids are concentrated in the channels of ancient rivers whose meandering patterns are preserved in the mapped occurrences of the CID. Some of these occurrences are expressed in the landscape as mesas representing locally inverted topography (Ramanaidou et al., 2003). Among these CID mesas is the ore-grade Mesa J of the Robe Pisolite (Robe Formation) in the vicinity of the Robe River of Western Australia (Ramanaidou et al., 2003).

Danišik et al. (2013) used the (U-Th)/He method to determine ages of crystallization of Fe (III) oxides in two samples of CID from a Mesa J drill core. The results indicated that the goethite-rich cortices of the “pelletoids” (ooids/pisoids) had an average age of $11.6_{(\pm 3.0)}$ Ma. In contrast, average ages of $14.3_{(\pm 3.7)}$ Ma and $18.3_{(\pm 3.5)}$ Ma were determined for hematite-rich centers (interiors/cores) of pelletoids from, respectively, the shallower and deeper core samples. Samples of goethite that replace wood range in age from about 7.0 to 9.4 Ma.

Danišik et al. (2013) discussed sources of error – including the possibility that the nominal radiometric ages represent minimum ages of crystallization, because the extent of post-crystallization loss of radiogenic ^4He was not assessed (e.g., Wolf et al., 1998; Shuster et al., 2005). Nevertheless, the (U-Th)/He ages of Danišik et al. (2013) indicate that the chemical weathering which produced the Fe(III) oxides in the CID of Mesa J was associated with the Miocene climate of western Australia.

The singular nature of the CID as features in the Australian landscape, their economic significance as iron ore, and their Miocene age invite questions about the paleoenvironmental conditions at the time of formation. Tardy et al. (1990) suggested that ferricrete/laterite formation is favored in environments with seasonally contrasting climates and average rainfall totaling ~ 1300 – 1700 mm/yr. The modern climate of western Australia is much drier. At Pannawonica, which is about 16 km from Mesa J and at a comparable elevation, average rainfall is only about 400 mm/yr (Australian Government Bureau of Meteorology). The contrast between modern rainfall totals and the annual rainfall totals that are thought to be necessary to the development of lateritic weathering systems suggests that further study of

the paleoenvironmental conditions associated with the formation of the oolitic CID should begin with the ancient meteoric waters.

The stable isotope ratios of hydrogen and oxygen in modern meteoric waters (rain or snow) are related to environmental parameters such as sources of input vapor, condensation histories, temporal and spatial changes of temperature, and in some situations, amounts of rainfall (e.g., Dansgaard, 1964; Friedman et al., 1964; Rozanski et al., 1993). Therefore, the stable isotope ratios of ancient meteoric waters are expected to have paleoenvironmental significance. This has been demonstrated for Pleistocene meteoric water preserved in groundwater and glacial ice (e.g., Plummer, 1993; EPICA Community Members, 2004; Person et al., 2007). However, actual samples of meteoric water older than the Pleistocene (e.g., Miocene) are not commonly preserved in the geologic record, and isotopic data for such waters are obtained from proxies.

A variety of studies have used hydrogen and/or oxygen isotopes in goethite and hematite as proxies of the isotopic composition of meteoric waters (Yapp, 1987, 1993, 1997, 2000, 2008; Bird et al., 1992, 1993; Girard et al., 1997, 2000, 2002; Bao and Koch, 1999; Bao et al., 1999, 2000; Pack et al., 2000; Poage et al., 2000; Sjostrom et al., 2004; Tabor et al., 2004a, 2004b; Tabor and Yapp, 2005; Seidel et al., 2005; Hren et al., 2006; Yapp and Shuster, 2011; Gulbranson et al., 2015). In such work, measured isotopic compositions of the Fe (III) oxides are combined with the relevant mineral-water isotopic fractionation factors ($^D\alpha$ or $^{18}\alpha$) to determine the isotopic composition of the waters. Confidence in the $\delta^{18}\text{O}$ of ancient waters estimated in this manner is reduced by questions about which of several published curves for the temperature dependence of the goethite-water oxygen isotope fractionation factor ($^{18}\alpha$) best mimics the oxygen isotope fractionations that occur under various circumstances in natural samples (e.g., Yapp, 1987, 1990, 2001, 2007; Zheng, 1998; Bao and Koch, 1999; Xu et al., 2002; Frierdich et al., 2015).

Use of hydrogen isotopes in goethite as the proxy for ancient water might circumvent this problem, because the goethite-water D/H fractionation factor ($^D\alpha$) seems to exhibit little, or no, variation with temperature over the range of temperatures found in chemical sedimentary systems on Earth (Yapp and Pedley, 1985; Yapp, 1987; Feng and Yapp, 2008). The work herein presents stable hydrogen isotope data and (U-Th)/He ages for ooid-rich CID samples in a drill core extracted from Mesa J near the Robe River in Western Australia. Isotopically constrained inferences about the hydrologic cycle in the subtropical Miocene climate of western Australia are discussed, as well as possible implications for the seasonal timing of iron (III) oxide crystallization.

2. SAMPLES AND ANALYTICAL METHODS

2.1. Sample location

Dr. E.R. Ramanaidou of CSIRO Exploration and Mining, Bentley, Western Australia, provided eight CID samples from a diamond drill core (CSIRO core J6087) that

was extracted from actively mined Mesa J of the Robe Formation in Western Australia (Ramanaidou et al., 2003). The drill site was at 21.736439 °S latitude, 116.244899 °E longitude. The site is about 70 km from the west coast of Australia (Fig. 1). At the time of drilling, the elevation of the local ground surface was 178 m (sea level datum). For this study, the samples from that core are labeled CID-2 with an additional number to indicate each of the eight samples in sequence, from the shallowest to the deepest (CID-2-1 is the shallowest, etc.). Sample depths are listed in Table 1. It should be mentioned that the core from which these eight CID-2 samples were obtained is not the core from which the two samples studied by Danišik et al. (2013) originated.

2.2. Sample characterization

Sample CID-2-6 in Fig. 2A illustrates the oolitic/pisolitic texture that is characteristic of these examples of CID at the hand-sample scale (Ramanaidou et al., 2003). Portions of each sample were separated and broken into smaller fragments. Several grams of handpicked oolitic fragments were subjected to successive ultrasonic treatments in de-ionized water to dislodge and suspend fine-grained, pore-lining material (Fig. 2A). After each treatment, the suspension was decanted, and the procedure was repeated until no additional material was dislodged. The residual oolitic/pisolitic fragments (“ultrasonic residue”) were powdered under reagent-grade acetone in an aluminum oxide mortar and pestle until the powder passed through a 63-micron brass sieve. At this stage of processing, the sieved ultrasonic residue is characterized as not chemically treated (nct).

Minerals in the ultrasonic residue (nct) were identified in the Huffington Department of Earth Sciences at Southern Methodist University (SMU) with X-ray powder diffraction (XRD) using a Rigaku Ultima III with Cu K α radiation. The extent of substitution of Al for Fe in the goethite was determined by the XRD method of Schulze (1984).

In addition, the chemical composition of pressed pellets of powdered and 0.5 M HCl-treated CID-2-7 and CID-2-8 were measured by X-ray fluorescence (XRF) on a Thermo Scientific ARL Perform’X Sequential XRF instrument in the Huffington Department of Earth Sciences at SMU. As discussed in a subsequent section, these chemical data were obtained for comparison with the expectations arising from the XRD spectra of the samples.

2.3. Hydrogen isotope analyses

Prior to stable isotope analysis, approximately 1–2 grams of the ultrasonic residue were treated for 16 h at room temperature (22 °C) with 40–45 ml of 0.5 M HCl. The HCl solution was then decanted, and the powder was thoroughly rinsed with successive aliquots of de-ionized water. The rinse procedure was considered to be complete if the pH of a 40–45 ml aliquot of rinse water did not change from its initial value (pH ~ 5.5) after at least 10 min of continuous contact with the sample. Each sample was then treated at room temperature with at least four successive aliquots of reagent-grade 30% H₂O₂ solution (each

aliquot 40–45 ml) for a total of 30 days (Yapp and Poths, 1991; Yapp, 1998). After the last aliquot of H₂O₂ was decanted, the sample was dried in a vacuum desiccator at room temperature with no additional rinsing with de-ionized water. Samples treated in the foregoing manner were termed “cleaned”.

Hydrogen isotope analysis of the CID-2 samples followed the procedure of Yapp and Pedley (1985), which is summarized briefly here. An aliquot of a cleaned sample was placed in a pure silica (“quartz”) glass boat, weighed, and loaded into a “quartz” glass dehydration chamber. After flushing the chamber for 3 min with pure O₂ gas, the chamber was closed, and the sample was outgassed at ~25 °C for 30 min, then 100 °C for 60 min in vacuum (Yapp and Pedley, 1985). Both CO₂ and H₂O were desorbed from the mineral surfaces during outgassing and were immediately frozen into a multiple-coil trap at liquid nitrogen temperatures. Desorbed CO₂ and H₂O from the 100 °C step were added to the gases from the 25 °C step in the multiple-coil trap. The H₂O and CO₂ were then cryogenically separated using a slush of dry ice and methanol. The very small amount of desorbed CO₂ (<1 micromole) was discarded, but the outgassed H₂O was quantitatively converted to H₂ by reaction with depleted uranium at 760 °C. A Toepler pump was used to collect and manometrically measure the yield of H₂ gas. Measured hydrogen yields have a precision of $\pm 1 \mu\text{mol}$. The hydrogen recovered from this procedure is designated Fraction 1 (Fr. 1), and a sample of CID that has been subjected to the procedure is described as “outgassed”.

The outgassed CID-2 sample remaining in the dehydration chamber was heated at 850 °C for 30 min in ~0.16 bar of pure O₂ (which converts goethite to hematite with loss of H₂O and small amounts of occluded CO₂). The evolved CO₂ and H₂O were frozen into a liquid nitrogen-cooled, multiple-coil trap and then cryogenically separated. The H₂O was quantitatively converted to H₂ (with measurement of hydrogen yield) using the same procedure as that outlined for Fraction 1. The H₂ collected from the dehydration step at 850 °C is designated Fraction 2 (Fr. 2) and contains the hydrogen from the structural hydroxyl in CID goethite. This H₂ was introduced into an evacuated sample tube and transferred to a Finnigan 252, dual-inlet, isotope ratio mass spectrometer for measurement of its δD value. δD is conventionally defined as:

$$\delta D = \left[\frac{(D/H)_{\text{sample}} - (D/H)_{\text{standard}}}{(D/H)_{\text{standard}}} \right] \times 1000\text{‰}$$

The standard is V-SMOW (hereafter referred to as SMOW). For analyzed duplicates of a sample, the overall uncertainty associated with extraction and isotopic measurement of the hydrogen is about $\pm 3\text{‰}$. All of the hydrogen extractions and D/H analyses were performed at SMU.

2.4. Oxygen isotope analysis of calcite

The $\delta^{18}\text{O}$ value of diagenetic calcite in sample CID-2-1 (Fig. 2B) was measured by the phosphoric acid method of McCrea (1950). Three aliquots of that sample were each reacted overnight (approximately 16 h) with 100% H₃PO₄

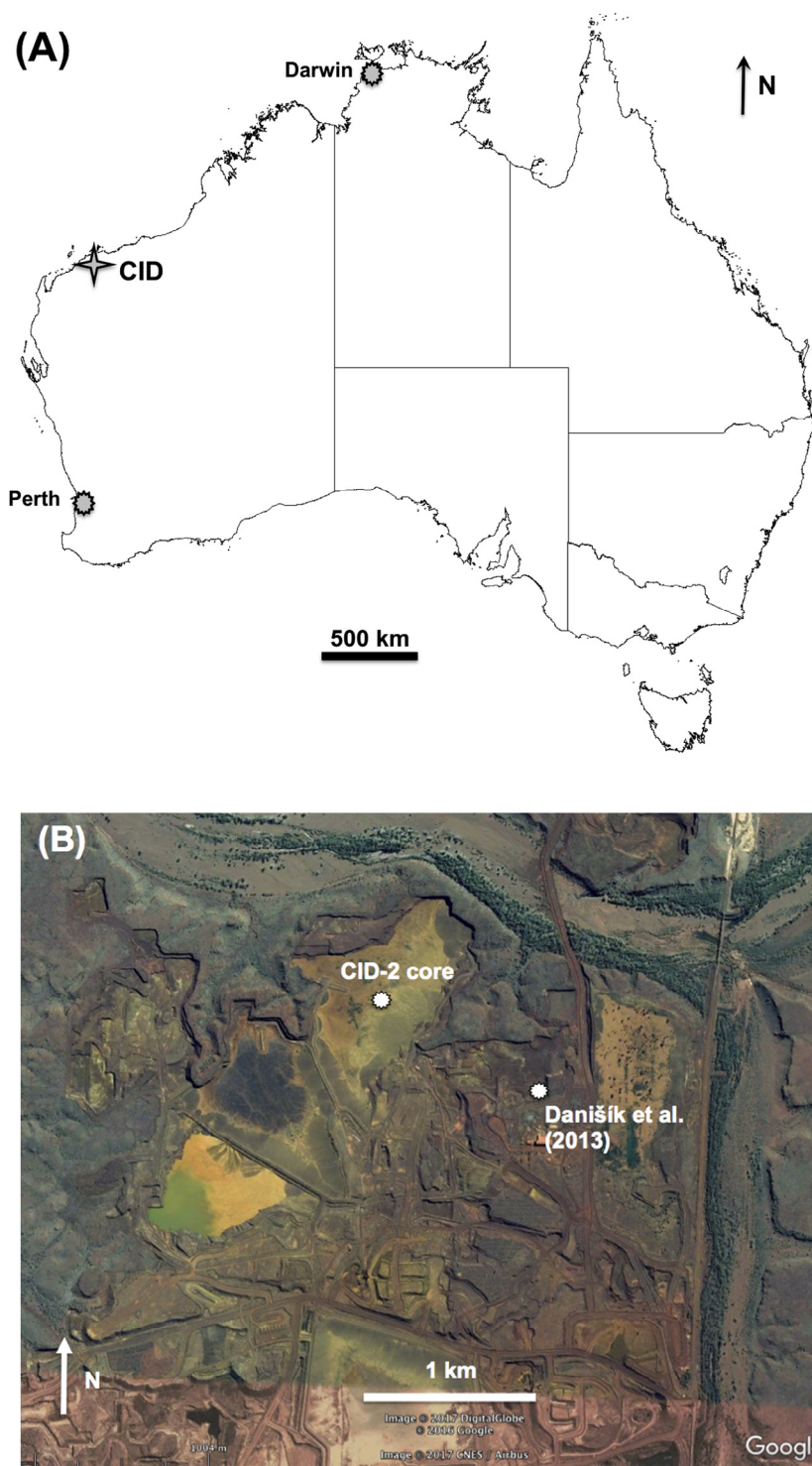


Fig. 1. (A) Outline map of Australia indicating the location of the Miocene channel iron deposit (CID) of the Robe Formation on Mesa J (4-pointed star) and the locations of the modern communities of Darwin and Perth, which are sites of IAEA precipitation stations. Darwin is situated at 12.46°S latitude and 130.84°E longitude (elevation ~36 m). Perth is at 31.95°S latitude and 115.97°E longitude (elevation ~17 m). (B) A satellite image from May, 2016 of the iron ore mine on Mesa J (source of image: Google, DigitalGlobe, CNES/Airbus). The dry, meandering channel of the Robe River is along the northern edge of the field of view. The CID-2 drill site was at 21.736439°S latitude, 116.244899°E longitude, and at a ground surface altitude of 178 m (sea level datum). The approximate locations of the CID-2 core and the core from which the samples of [Danišik et al. \(2013\)](#) were taken are marked in the figure. As seen in the image, ore has been removed from those location.

Table 1
Depths of CID-2 samples in the drill core and minerals detected by XRD.

Sample	Depth (m)	Minerals ^a
CID-2-1	5.0	Gt, Hm, Qtz, Cc
CID-2-2	12.0	Gt, Hm, Qtz
CID-2-3	15.4	Gt, Hm, Qtz
CID-2-4	19.5	Gt, Hm, Qtz
CID-2-5	25.8	Gt, Hm, Qtz
CID-2-6	31.2	Gt, Hm, Qtz
CID-2-7	33.2	Gt, Hm, Qtz
CID-2-8	36.2	Gt, Hm, Qtz

^a Gt = goethite; Hm = hematite; Qtz = quartz; Cc = calcite.

at 25 °C. The yield of CO₂ gas was measured manometrically, followed by transfer to a Finnigan 252, dual inlet, isotope ratio mass spectrometer for measurement of the δ¹⁸O value.

2.5. (U-Th)/He analyses

To avoid analyzing samples affected by pore spaces in the CID, approximately microgram-sized aliquots were removed from ooids positioned within tight clusters. It is not known to what extent the proportions of the minerals in the “micro-aliquots” analyzed for (U-Th)/He mimic the proportions of minerals in the powdered, gram-size aliquots of ultrasonic residue that were prepared for the combination of XRD, XRF, and light element stable isotope analyses.

All measurements for (U-Th)/He were made at the Noble Gas Thermochronometry Lab of the Berkeley Geochronology Center following analytical methods described in Shuster et al. (2012), Vasconcelos et al. (2013), and Deng et al. (2017). Each aliquot was placed into a niobium capsule. Under ultra high vacuum, the sample was heated to 950 °C (±5 °C) using a diode laser that was focused on the capsule. The temperature was controlled using calibrated optical pyrometry. After purification of the extracted gas, a known molar abundance of ³He was added to the gas, and the molar abundance of ⁴He in the sample was measured by isotope dilution using quadrupole mass spectrometry. After measurement of the ⁴He, the capsule was transferred to a Teflon vial, spiked with known molar abundances of ²³³U, ²²⁹Th and Sm enriched in ¹⁴⁷Sm, then dissolved in concentrated HCl at 90 °C for 12 h. The solution was dried down on a hot plate, re-dissolved in a mixture of concentrated HNO₃ and HF for 1 h, and diluted to a running solution of 5% HNO₃ and 0.6% HF for analysis. Molar abundances of ²³⁸U, ²³²Th, and ¹⁴⁷Sm in the sample were measured by isotope dilution using ICP-MS. Relative analytical errors are typically about ±2% of the nominal value. The original intent of the (U-Th)/He analyses was the straightforward determination of radiometric ages. Inasmuch as the masses of the analyzed aliquots are not needed for that purpose, they were not measured (e.g., Danišik et al., 2013).

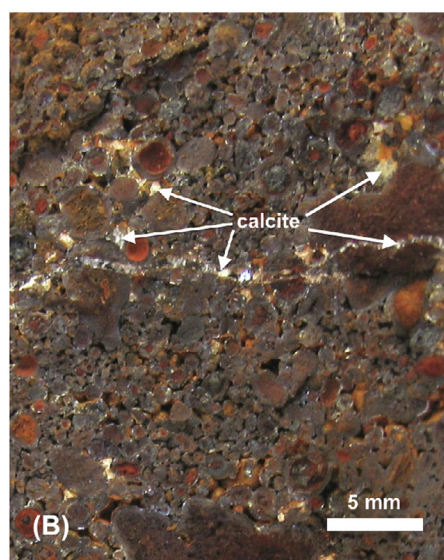
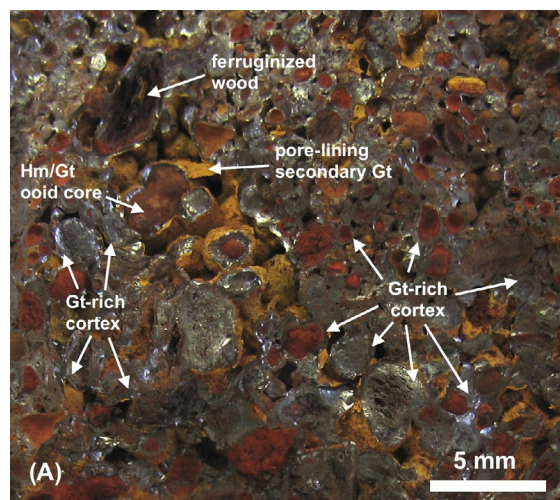


Fig. 2. Hand samples of CID from the Robe Formation of Mesa J. (A) Photograph of sample CID-2-6 illustrating the characteristic oolitic/pisolitic texture of these channel iron deposits (CID). Arrows indicate examples of some of the textural components of the CID-2 samples—goethite-rich cortices of ooids, core of an ooid, a piece of ferruginized wood, and the thin coating of ocherous, pore-lining secondary goethite in this sample. Gt = goethite, and Hm = hematite. Many of the cortices exhibit a quasi-metallic/vitreous luster. (B) Photograph of oolitic sample CID-2-1 showing the pore-filling and fracture-filling calcite of that sample. (see Fig. 3). No quartz grains are discernible in these photos.

2.6. ⁴He/³He analyses

Two samples, one with a high proportion of goethite (CID-2-3) and the other with a low proportion of goethite (CID-2-4), were irradiated over a continuous 5-h period with protons that had an incident energy of ~220 MeV and a total fluence of ~1 × 10¹⁶/cm². The irradiation was performed at the Francis H. Burr Proton Therapy Center at Massachusetts General Hospital, Boston, MA, USA, and produced an abundance of spallation ³He throughout

all phases in the samples with a spatial distribution that is likely uniform (Shuster et al., 2004, 2005).

To quantify possible post-crystallization diffusive loss of radiogenic ^4He from the Fe (III) oxides, stepwise degassing analyses of $^4\text{He}/^3\text{He}$ were conducted on these irradiated samples (Shuster et al., 2005). Each was heated stepwise under ultra-high vacuum to recover evolved He. The durations of the various steps were between ~ 0.3 and 3.0 h, and the temperature of each step was controlled to within $\pm 5^\circ\text{C}$. The He accumulated at each step was purified, and the $^4\text{He}/^3\text{He}$ ratio and molar abundance of ^3He were analyzed using a MAP 215-50 sector-field mass spectrometer calibrated with known molar abundances of reference gases (further analytical details can be found in Tremblay et al., 2015). Small corrections are made for blank ^4He and for ^4He produced during proton irradiation (by assuming a production ratio of $^4\text{He}/^3\text{He} = 10$). At each degassing step, an apparent “step age” is calculated by dividing each observed $^4\text{He}/^3\text{He}$ ratio by the bulk $^4\text{He}/^3\text{He}$ ratio (calculated from the sum of all steps), and multiplying by the mean (U-Th)/He age of the sample (Shuster and Farley, 2005).

3. RESULTS

3.1. Mineral identification

The XRD spectra of the eight CID-2 samples are shown in Fig. 3. For seven of the eight samples, the only XRD-detectable minerals were goethite, hematite, and quartz (Fig. 3 and Table 1). The single exception, CID-2-1, also contained calcite (Fig. 3; Table 1), which occurred as veins and pore-filling material (Fig. 2B).

3.2. Calcite $\delta^{18}\text{O}$

On the V-PDB scale (hereafter PDB), the average $\delta^{18}\text{O}$ value of the calcite in the three analyzed aliquots of the CID-2-1 sample was $-7.1_{(\pm 0.1)}\text{‰}$. This corresponds to a $\delta^{18}\text{O}$ value of $+23.6\text{‰}$ on the SMOW scale (Coplen et al., 1983).

3.3. (U-Th)/He data

Moles of ^{238}U , ^{232}Th , ^4He , and ^{147}Sm measured in various aliquots of the CID samples are reported in Table 2 together with the calculated (U-Th)/He ages. The ages listed in Table 2 do not account for possible post-crystallization loss of ^4He by diffusion or alpha recoil (e.g., Shuster et al., 2005). The effects of ^4He loss by alpha recoil were presumably mitigated by sampling the interiors of aggregates of CID-2 ooids—i.e., away from sample surfaces and pore spaces (e.g., Shuster et al., 2005; Vasconcelos et al., 2013). The absence of calculated adjustments for possible diffusive loss of ^4He from the CID-2 samples of this work implies that the nominal ages of Table 2 may underestimate the actual ages of crystallization. However, use of these nominal ages facilitates comparison with the Mesa J results of Danišik et al. (2013), which also lack such adjustments.

The ages in Table 2 range from 2.7 Ma to 30.2 Ma among the aliquots of the different CID-2 samples. The molar Th/U ratios range from 0.42 to 5.70. Note that the minimum Th/U ratio (0.42) and the maximum Th/U ratio (5.70) in Table 2 were measured for two aliquots of the same sample (aliquots CID-2-8-S and CID-2-8-R, respectively).

3.4. $^4\text{He}/^3\text{He}$ results from CID-2-3 and CID-2-4

Results from stepwise degassing measurements of He in CID-2-3 and CID-2-4 are reported in Table S1 and shown in Figs. 4 and 5. Both samples reveal: (i) young apparent step ages (< 1 Ma) in the initial few percent of released ^3He , (ii) a systematic increase in step ages over the next tens of percent of released ^3He , and (iii) a following sequence of steps that exhibit an approximate “plateau” age. The plateau increments constitute at least 50% of the total ^3He released in the stepwise heating. The final $\sim 10\%$ of the ^3He released from CID-2-3 reveals a systematic increase in apparent ages, whereas the final step ages from CID-2-4 remain invariant to within estimated uncertainty. Error-weighted mean ages calculated from the plateau steps are 8.35 ± 0.34 Ma (CID-2-3) and 25.5 ± 1.9 Ma (CID-2-4).

3.5. H_2 yields, δD , and substituent Al

The measured initial mass (m_i) and the outgassed mass (m_o) of each analyzed aliquot of CID, the water yields from Fr. 1 and Fr. 2 (measured as micromoles of H_2), and the δD values determined for the H_2 of Fr. 2 are listed in Table 3. The outgassed mass is defined as $m_o = m_i - m_{100}$. Where, m_{100} = the mass of H_2O desorbed in vacuum at 25 and 100°C in Fr. 1 (calculated from micromoles of H_2 in Fr. 1). Measured δD values of H_2 in Fr. 2 range from -150‰ to -138‰ (Table 3).

The mole fraction (y_{Al}) of Al substituted for Fe in the CID goethite as determined by the method of Schulze (1984) is also reported in Table 3. Values of y_{Al} range from a low of 0.02 for goethite in CID-2-1 to a high of 0.11 for goethite in CID-2-4. Substituent Al in goethite is expected to have a systematic effect on the mineral-water isotopic fractionation for both hydrogen and oxygen (Yapp, 1993, 2012; Feng and Yapp, 2008). Therefore, the measured δD values of Al-substituted goethites were adjusted to represent the δD of the FeOOH end-member.

The Al-adjusted δD values were determined as follows. For each increase of 0.01 in the mole fraction of substituent Al in goethite, the measured δD value was decreased by 1‰ to estimate the δD of the end-member FeOOH (Feng and Yapp, 2008). Therefore, a one-standard-deviation uncertainty of ± 0.01 in the mole fraction of Al corresponds to an uncertainty in an Al-adjusted δD value of about $\pm 1\text{‰}$. The Al-adjusted δD values range from -154‰ to -143‰ among the aliquots of CID samples in Table 3.

The sample depths and Al-adjusted δD values for the eight CID-2 samples are in Table 4. For samples with more than one analyzed aliquot, the δD value listed in Table 4 is the average of individual δD values listed in Table 3. The range of δD values in Table 4 is comparatively small (from

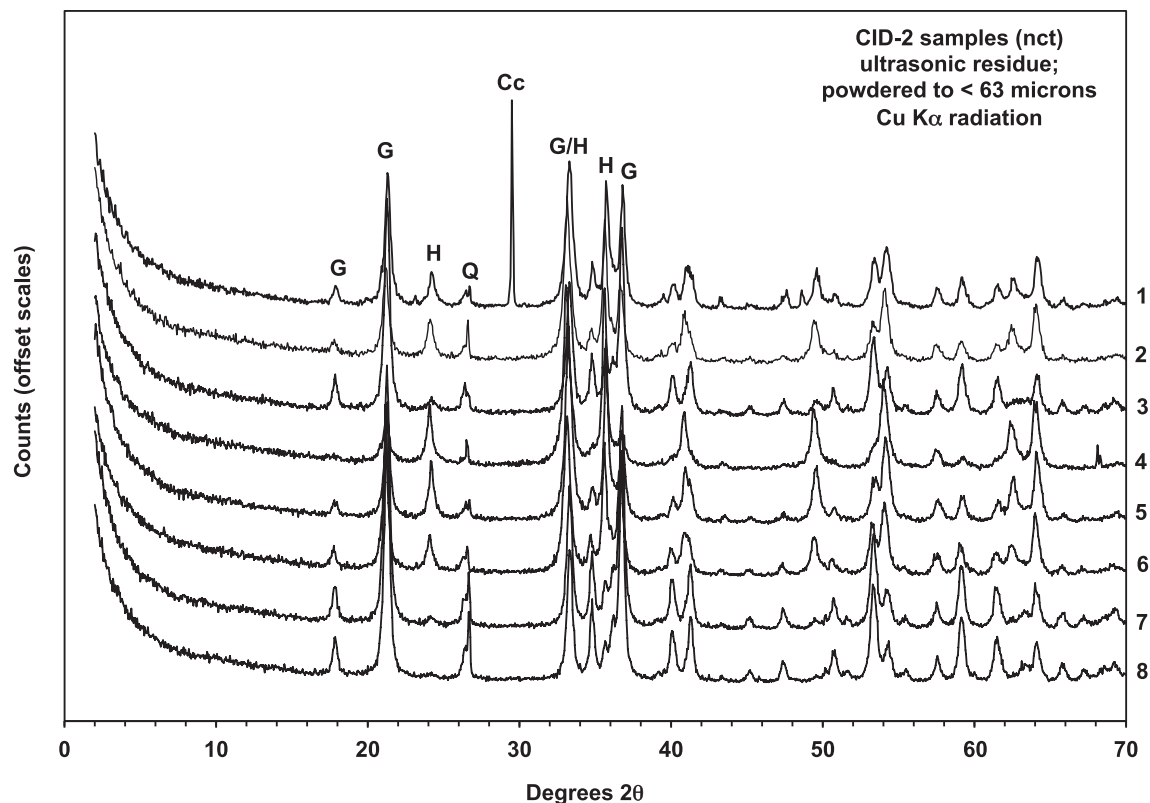


Fig. 3. X-ray diffraction (XRD) spectra of powdered “ultrasonic residue” of the eight CID samples of this study (see text). The samples were not chemically treated (nct) prior to these XRD measurements. The number to the right of each spectrum refers to the sample represented by that spectrum (“1” corresponds to CID-2-1, etc.). Some of the principal XRD peaks of the minerals are labeled. In this figure, G = goethite; H = hematite; Q = quartz; Cc = calcite. With one exception, goethite, hematite, and quartz are the only XRD-detectable minerals in these samples. The single exception is sample CID-2-1, which also contains calcite (Also see Fig. 2B and Table 1).

Table 2
(U-Th)/He analyses and calculated ages of CID-2 samples.

Sample	Age (Ma)	Error (Ma)	^{238}U (mol)	^{232}Th (mol)	Th/U	^{147}Sm (mol)	^4He (mol)
CID-2-1-T	11.6	0.2	8.685E-14	1.495E-13	1.72	5.831E-14	1.751E-15
CID-2-1-S	8.0	0.2	5.306E-14	5.288E-14	1.00	2.714E-14	7.004E-16
CID-2-1-R	11.2	0.3	2.954E-13	4.399E-13	1.49	1.271E-13	5.778E-15
CID-2-2-S	13.2	0.4	5.095E-14	1.229E-13	2.41	4.465E-14	1.401E-15
CID-2-2-R	12.5	0.3	2.171E-14	4.115E-14	1.90	2.627E-14	5.253E-16
CID-2-3-T	8.2	0.2	3.449E-14	4.062E-14	1.18	2.889E-14	5.253E-16
CID-2-3-S	7.7	0.1	1.348E-13	8.440E-14	0.63	5.866E-14	1.576E-15
CID-2-3-R	6.7	0.4	3.099E-14	1.996E-14	0.64	2.066E-14	3.502E-16
CID-2-4-T	30.2	3.1	6.654E-15	2.977E-14	4.47	1.086E-14	5.253E-16
CID-2-4-S	20.8	0.5	2.521E-14	1.145E-13	4.54	1.926E-14	1.401E-15
CID-2-4-R	15.7	0.8	8.317E-14	4.206E-13	5.06	6.619E-14	3.677E-15
CID-2-5-T	9.1	0.2	7.617E-14	1.168E-13	1.53	2.977E-14	1.226E-15
CID-2-5-S	16.6	0.3	5.446E-14	1.192E-13	2.19	3.572E-14	1.751E-15
CID-2-5-R	8.7	0.1	2.542E-13	5.565E-13	2.19	7.442E-14	4.202E-15
CID-2-6-S	15.1	0.5	1.208E-14	2.574E-14	2.13	1.541E-14	3.502E-16
CID-2-6-R	12.8	0.4	1.401E-14	2.416E-14	1.73	1.593E-14	3.502E-16
CID-2-7-R	7.8	0.1	6.776E-14	9.508E-14	1.40	1.944E-14	8.755E-16
CID-2-8-S	10.0	0.6	2.556E-14	1.068E-14	0.42	1.418E-14	3.502E-16
CID-2-8-R	2.7	0.1	6.829E-14	3.892E-13	5.70	2.819E-14	5.253E-16

The descriptors “R, S, and T” after each sample designation are references to different analyzed aliquots of that sample. Relative analytical error for the moles (mol) of the isotopic species is about $\pm 2\%$ of the nominal value. Propagated analytical error for each nominal age is shown in the table.

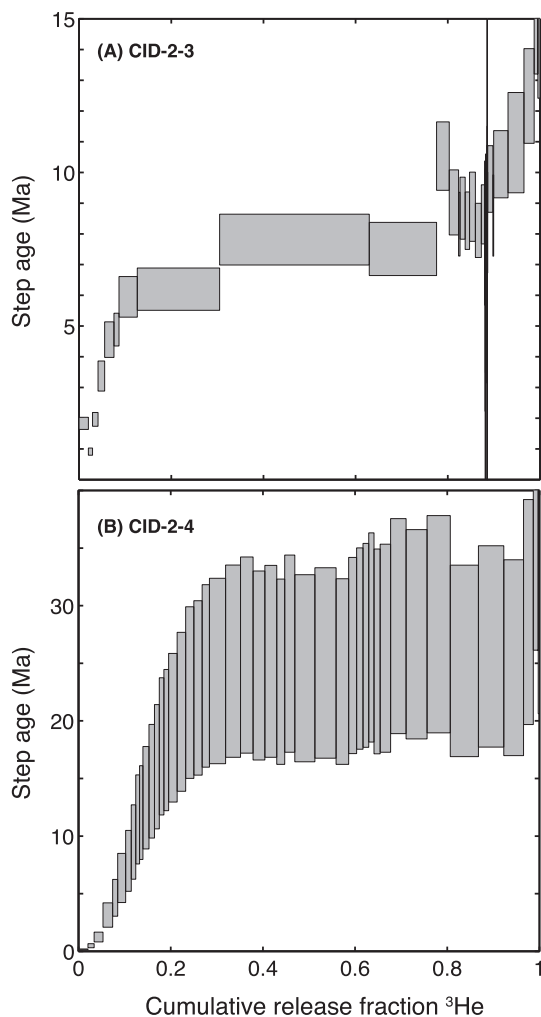


Fig. 4. $^4\text{He}/^3\text{He}$ age spectra from stepwise degassing analyses of (A) CID-2-3 and (B) CID-2-4 (see text and Table S1). The step ages are calculated as the product of the bulk-normalized $^4\text{He}/^3\text{He}$ ratio at each step and the bulk (U-Th)/He age of the sample (Shuster and Farley, 2005). For CID-2-3 there is a plateau age of $8.35_{(\pm 0.34)}$ Ma, whereas for CID-2-4, the plateau age is $25.5_{(\pm 1.9)}$ Ma. The estimated uncertainties include analytical uncertainties in $^4\text{He}/^3\text{He}$ ratios and standard deviation in (U-Th)/He ages of separate aliquots shown in Table 2.

–153‰ to –146‰) and the δD exhibit no systematic pattern of variation with depth.

3.6. Goethite—relative abundance

Table 4 also lists the Al-adjusted molecular weight (M_G) of the goethite in each CID sample. These M_G values were calculated using the values of γ_{Al} in Table 3 and reflect the effects of substituent Al on the molar mass of goethite, where the formula for goethite is represented as $\text{Fe}_{(1-y)}\text{Al}_y\text{OOH}$.

Goethite is the only hydroxyl-bearing mineral detectable in the XRD spectra of Fig. 3 and relative peak heights in those spectra suggest that the proportion of goethite varies among the samples. To obtain an initial estimate of the pro-

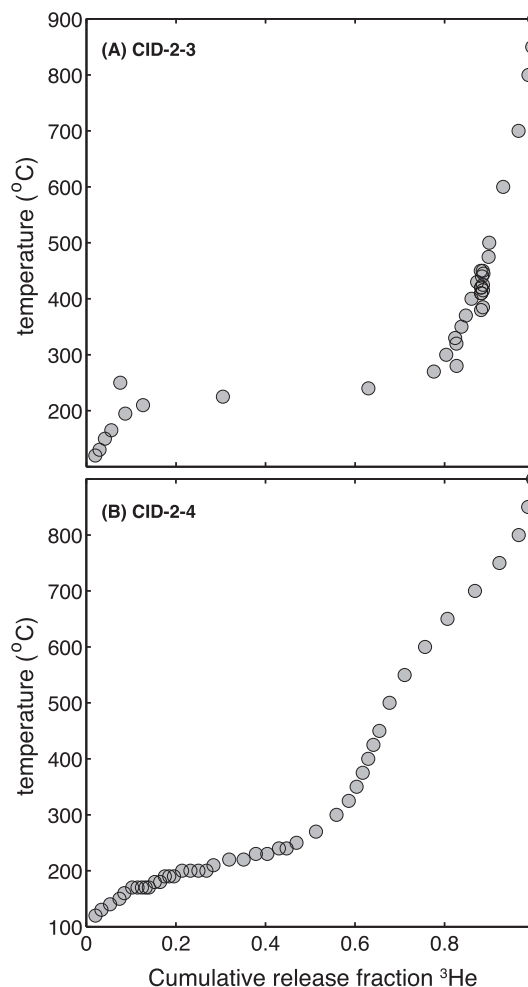


Fig. 5. Cumulative fraction of ^3He released by stepwise heating of (A) CID-2-3 and (B) CID-2-4. Note the increase in the rate of loss of ^3He at ~ 200 °C in each sample, indicating the early stages of the solid state goethite to hematite phase transition (see text and Table S1).

portion of goethite in each sample, it was assumed that the hydrogen in Fraction 2 was derived only from stoichiometric hydrogen in goethite. Thus, the apparent mass of goethite (m_G) in a sample was calculated from the combination of (1) the water yield of Fr. 2 (measured as micromoles of H_2) and (2) the value of M_G for that sample (see Tables 3 and 4). Then, $m_G = 2n_{\text{Fr}2} M_G$, where $n_{\text{Fr}2}$ = moles of H_2O in Fraction 2. Now, $w_G = m_G/m_o$, and w_G is the apparent mass fraction of goethite in the sample.

Values of w_G calculated in this manner range from a low of about 0.38 to a high of 1.02–1.03. The latter two values were determined for CID-2-8 and one of the three aliquots of CID-2-7 in Table 2 (lab #2749). Values of $w_G > 1.00$ are obviously an overestimate of the proportion of goethite in a sample and suggest that some of the hydrogen in Fr. 2 of these samples was derived from “high temperature non-stoichiometric water” (HTNW) that is not outgassed from goethite at 100 °C (Yapp and Poths, 1995; Boily et al., 2006). The amounts of HTNW in CID-2-7 and CID-2-8

Table 3

Mass of analyzed aliquot, water yield (measured as H₂), mole fraction of substituent Al and δD of goethite in CID-2 samples.

Sample	lab #	^a <i>m_i</i>	^b <i>m_o</i>	H ₂ O (Fr. 1)	H ₂ O (Fr. 2)		<i>y</i> _{Al}	Al-adjusted
		(mg)	(mg)		(μ mol)	(μ mol)		
CID-2-1	2078	46.2	<i>45.6</i>	36	176	−145	0.02	−147
CID-2-2	2095	71.1	<i>70.2</i>	49	232	−142	0.05	−147
CID-2-3	2081	56.6	<i>55.8</i>	46	292	−142	0.06	−148
CID-2-4	2093	95.5	<i>94.2</i>	72	211	−143	0.11	−154
CID-2-4	2094	91.1	<i>89.9</i>	64	203	−138	0.11	−149
CID-2-5	2096	53.2	<i>52.5</i>	39	171	−147	0.06	−153
CID-2-6	2077	38.4	<i>37.8</i>	31	140	−150	0.04	−154
CID-2-6	2091	45.2	<i>44.4</i>	43	214	−143	0.04	−147
CID-2-7	2079	46.2	<i>45.6</i>	32	260	−146	0.03	−149
CID-2-7	2087	53.0	<i>52.3</i>	41	278	−140	0.03	−143
CID-2-7	2749	40.7	<i>40.2</i>	30	234	−143	0.03	−146
CID-2-8	2092	48.9	<i>48.3</i>	36	282	−146	0.06	−152

Fraction 1 (Fr. 1) is the micromoles of water (measured as H₂; see text) collected during outgassing of the sample at 25 °C and 100 °C in vacuum. Fraction 2 (Fr. 2) is the micromoles of water (measured as H₂) recovered from dehydration of the sample at 850 °C in ~0.16 bar of pure O₂ (see text).

*y*_{Al} is the substituent Al in goethite as a mole fraction of Al + Fe in goethite. *y*_{Al} was determined by the XRD method of Schulze (1984). *y*_{Al} has a one-standard-deviation uncertainty of ± 0.013 .

The “Al-adjusted” δD value of goethite is shown in bold. The Al-adjusted δD value was obtained as follows. For each 0.01 mol fraction of substituent Al in goethite, the measured δD value was decreased by 1‰ to estimate the δD of the end-member FeOOH (Feng and Yapp, 2008). The uncertainty in an Al-adjusted δD value arising from a one-standard-deviation uncertainty in the mole fraction of Al is about $\pm 1\%$.

^a *m_i* = initial total mass (mg) = the measured mass of the aliquot of sample prior to outgassing in vacuum at 100 °C.

^b *m_o* = outgassed mass of the sample (mg) = the mass of the aliquot of the CID sample after subtracting the mass of H₂O in Fr. 1 from the initial mass of the aliquot are indicated by the values in italics.

Table 4

Sample depth, Al-adjusted molecular weight of goethite, mass fraction of goethite in the sample, average (U-Th)/He age, Th/U ratio, and δD of the FeOOH end-member.

Sample	^a depth (m)	^b <i>M_G</i>	^c <i>W_G</i>	^d <i>t_m</i> (Ma)	^e Th/U	^f δD (‰)
CID-2-1	5.0	88.4	0.64	10.3 (± 2.0)	1.40	−147
CID-2-2	12.0	87.6	0.55	12.9 (± 0.5)	2.15	−147
CID-2-3	15.4	87.3	0.86	7.5 (± 0.8)	0.82	−148
CID-2-4	19.5	85.8	0.36	22.2 (± 7.3)	4.69	−152
CID-2-5	25.8	87.3	0.54	11.4 (± 4.4)	1.97	−153
CID-2-6	31.2	87.8	0.62	14.0 (± 1.6)	1.93	−150
CID-2-7	33.2	88.1	0.93	7.8	1.40	−146
CID-2-8	36.2	87.3	0.96	6.3 (± 5.1)	3.06	−152

^a Depth of core sample (in meters) below the local ground surface.

^b *M_G* is the approximate gram-formula weight (gm/mole) of goethite after accounting for the change in molecular weight associated with substitution of Al for Fe in goethite.

^c *W_G* = *m_G**/*m_S** See text.

^d *t_m* = the average (U-Th)/He age of the mixture and the subscripted error of the mean (with one exception). The exception is the age for CID-2-7, which represents a single analysis (see Table 2).

^e Th/U is the average value of the Th/U molar ratios reported for each sample in Table 1 (with the exception of CID-2-7 for which there was only a single analysis).

^f Average Al-adjusted δD value is reported if multiple analyses of a sample were available (see Table 3).

can be estimated from their chemical compositions, because there is almost no XRD-detectable hematite in those samples (Fig. 3).

3.7. Chemical composition of CID-2-7 and CID-2-8

Results of the XRF and dehydration analyses of CID-2-7 and CID-2-8 are reported in Table 5 as the mole fractions

[*x*(*i*)] of the indicated oxide components. The mole fraction of H₂O in Table 5 was determined using the yield of hydrogen in Fr. 2 in combination with the abundances of the other oxide components (as determined from XRF). Relative error (counting statistics) of the XRF data is about $\pm 0.1\%$ of the nominal value. Taken together, the Fe₂O₃, H₂O, SiO₂ and Al₂O₃ components constitute over 99% of these samples (Table 5).

Table 5
Chemical analysis of pressed pellets of powdered, 0.5 M HCl-treated CID-2-7 and CID-2-8.

Oxide (i)	CID-2-7 $x(i)$	CID-2-8 $x(i)$
Fe ₂ O ₃	0.434	0.425
P ₂ O ₅	0.0006	0.0004
Al ₂ O ₃	0.0207	0.0175
K ₂ O	0.0001	0.0001
TiO ₂	0.0010	0.0018
MnO	0.0015	0.0019
Na ₂ O	0.0011	0.0008
SiO ₂	0.052	0.076
CaO	0.0006	0.0004
MgO	0.0038	0.0035
H ₂ O	0.485	0.473
Sum	1.000	1.000

$x(i)$ = mole fraction of the indicated oxide (i). The value for $x(\text{H}_2\text{O})$ in the table was determined from the yield of Fr. 2 reported in Table 3. All other $x(i)$ values were determined by XRF analysis (see text).

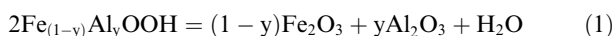
4. DISCUSSION

4.1. HTN hydrogen in goethite

High temperature nonstoichiometric (HTN) hydrogen is excess, non-structural hydrogen (as H₂O) – i.e., HTNW – that remains in goethite even after outgassing the sample at 100 °C in vacuum (Yapp and Poths, 1995). HTN hydrogen rapidly exchanges D/H with ambient water vapor at room temperature—a characteristic that contrasts with the apparently non-exchangeable structural, stoichiometric hydrogen in goethite (Yapp and Poths, 1995; Yapp, 1997; Feng and Yapp, 2008; Yapp and Shuster, 2011). Therefore, the HTN hydrogen in a goethite sample as a mole fraction (f_{HTN}) of the total hydrogen in the outgassed goethite is germane to the current study, because the measured δD of the goethite (δD_{meas}) would represent a two-component mixture of non-exchangeable structural hydrogen (δD_{struc}) and exchangeable HTN hydrogen (δD_{HTN}).

An estimate of the proportion of HTNW in the goethite can be made from knowledge of the chemical composition of CID-2 samples that contain only goethite and quartz – a condition approximated by CID-2-7 and CID-2-8 (Fig. 3). The following discussion assumes that there is no Al in quartz.

For goethite expressed as Fe_(1-y)Al_yOOH, a simple dehydration reaction illustrates the expected proportions of the Fe and Al oxide components in the mineral.



Thus, if $x(i)$ is the mole fraction of an oxide component “ i ” in a mixture of goethite and quartz, the stoichiometric hydrogen in goethite as a mole fraction [$x(\text{H}_2\text{O})_{\text{stoich}}$] of all the oxide components is:

$$x(\text{H}_2\text{O})_{\text{stoich}} = x(\text{Fe}_2\text{O}_3) + x(\text{Al}_2\text{O}_3) \quad (2)$$

The mole fraction of HTNW in samples CID-2-7 and CID-2-8 may be determined from the data in Table 5 as follows:

$$x(HTNW) = x(\text{H}_2\text{O})_{\text{total}} - x(\text{H}_2\text{O})_{\text{stoich}} \quad (3)$$

After substituting into Eqn. (3) from Eqn. (2),

$$x(HTNW) = x(\text{H}_2\text{O})_{\text{total}} - [x(\text{Fe}_2\text{O}_3) + x(\text{Al}_2\text{O}_3)] \quad (4)$$

where, $x(\text{H}_2\text{O})_{\text{total}}$ = the mole fraction for H₂O entered in Table 5. For CID-2-7, $x(HTNW) = 0.0303$ and for CID-2-8, $x(HTNW) = 0.0305$.

Now, let f_{HTN} = the moles of HTNW as a decimal fraction of the total moles of water evolved from the sample at 850 °C in Fr. 2. Then,

$$f_{HTN} = \frac{x(HTNW)}{x(\text{H}_2\text{O})_{\text{total}}} \quad (5)$$

For CID-2-7, $f_{HTN} = \frac{0.0303}{0.485} \approx 0.06$ and for CID-2-8, $f_{HTN} = \frac{0.0305}{0.473} \approx 0.06$

Note that f_{HTN} has the same magnitude whether it is expressed as a ratio of moles of water (H₂O) or moles of hydrogen atoms (H). Therefore, high temperature non-stoichiometric hydrogen (HTNW) seems to constitute about 6% of the total hydrogen recovered in Fr. 2 for both CID-2-7 and CID-2-8.

Some insight into the robustness of the aforementioned values of f_{HTN} can be gleaned from a comparison of XRD-derived values of y_{Al} with values of y_{Al} determined from the XRF results of Table 5, where:

$$y_{\text{Al}} = \frac{x(\text{Al}_2\text{O}_3)}{x(\text{Al}_2\text{O}_3) + x(\text{Fe}_2\text{O}_3)} \quad (6)$$

For CID-2-7, $y_{\text{Al}}(\text{XRF}) = 0.05$ and $y_{\text{Al}}(\text{XRD}) = 0.03$. For CID-2-8, $y_{\text{Al}}(\text{XRF}) = 0.04$ and $y_{\text{Al}}(\text{XRD}) = 0.06$. For a particular sample, the values of y_{Al} determined by the two methods are analytically indistinguishable. This suggests that the XRF-derived oxide compositions of Table 5 are usefully accurate and gives credence to the f_{HTN} value calculated for the goethite of CID-2-7 and CID-2-8.

At natural abundance levels $\text{D} \ll \text{H}$, and the measured δD (δD_{meas}) for a two-component mixture of HTN hydrogen (δD_{HTN}) and structural hydroxyl hydrogen (δD_{struc}) is expressed by the following equation:

$$\delta D_{\text{meas}} = f_{HTN}\delta D_{HTN} + (1 - f_{HTN})\delta D_{\text{struc}} \quad (7a)$$

$$[\delta D_{\text{meas}} - \delta D_{\text{struc}}] = f_{HTN}[\delta D_{HTN} - \delta D_{\text{struc}}] \quad (7b)$$

The δD_{struc} of goethite is the parameter of interest for discussion of ancient environments, and the difference between δD_{meas} and δD_{struc} depends upon the magnitude of f_{HTN} and the difference between δD_{HTN} and δD_{struc} (Eq. (7b)). For $f_{HTN} = 0.06$, a difference between δD_{HTN} and δD_{struc} as large as 100‰ would result in a difference of 6‰ between δD_{meas} and δD_{struc} .

Therefore, some of the analytical uncertainty of $\pm 3\%$ observed for the CID-2 samples may arise from the effects of HTNW in the goethite. However, for an SMU “reference” goethite with essentially no HTNW, the one-standard-deviation precision for δD measurements over an interval of more than two decades is $\pm 2\%$. Thus, the

δD values reported in [Tables 3 and 4](#) should credibly represent the D/H of structural hydrogen in the goethite of samples CID-2-7 and CID-2-8.

The presence of significant hematite ([Fig. 3](#)) precludes the straightforward use of chemical analyses to calculate f_{HTN} values for the goethite in most of the CID-2 samples. However, if the f_{HTN} value of 0.06 determined for the goethite of CID-2-7 and CID-2-8 is applicable to all of the goethite samples in this study, the measured δD values of the CID-2 goethites should be representative of the structural hydrogen. Constancy of the f_{HTN} value among the goethites of the CID-2 samples is assumed in subsequent discussion.

4.2. Goethite—HTNW-compensated abundance

If $f_{HTN} = 0.06$, it implies that 94% of the water recovered in Fr. 2 of the analyzed aliquots in [Table 3](#) is stoichiometric and therefore appropriate for use in calculating the mass of goethite. Let $m_G^* = 2(n_{Fr2} - n_{HTNW})M_G =$ HTNW-compensated mass of goethite. Also, let $m_S^* = m_o - m_{HTNW}$. Where, m_{HTNW} = mass of the HTNW, n_{HTNW} = moles of the HTNW, and M_G = gram-formula weight (“molecular weight”) of the goethite. Then, $W_G = m_G^*/m_S^*$, where W_G is the HTNW-compensated mass fraction of goethite in a sample. Values of W_G are included in [Table 4](#) and range from 0.36 to 0.96. For the CID-2 samples, this range is physically reasonable given the presence of various proportions of hematite and small amounts of nominally anhydrous quartz ([Fig. 3](#)). Consequently, W_G is presumed to be more accurate than w_G as a measure of the mass fraction of goethite in each analyzed aliquot, and W_G is used henceforth.

4.3. (U-Th)/He ages of the CID-2 samples

4.3.1. “Anomalous” aliquot CID-2-8-R

Aliquot “R” of goethite-rich sample CID-2-8 ($W_G = 0.96$) has a Th/U ratio of 5.70, which is the highest value in [Table 2](#) and distinctly higher than the Th/U ratios in other goethite-rich samples of CID (e.g., CID-2-3, CID-2-7). Moreover, the Th/U ratio of 5.70 in CID-2-8-R contrasts with a Th/U ratio of 0.42 for aliquot CID-2-8-S ([Table 2](#)). In addition, CID-2-8-R has the youngest apparent age ($t_m = 2.7$ Ma) of any of the aliquots of [Table 2](#) ([Fig. 6A](#)). A speculative explanation of the CID-2-8-R results in [Fig. 6A](#) and B derives from the association of its high Th/U ratio with its relatively young, apparent radiometric age.

Goethite-rich sample CID-2-8 is the deepest (36.2 m) in the suite of samples from this core ([Table 1](#)). Thus, it has probably had the best chance of being in prolonged contact with groundwater. Such contact might have promoted post-accumulation, microbially mediated dissolution of some Fe (III) oxide (e.g., [Hersman et al., 1996, 2001; Grantham et al., 1997; Morris and Ramanaidou, 2007](#)). If so, insoluble Th ([Neck et al., 2003](#)) from the dissolved Fe(III) oxide could have been deposited in the locally affected volume of CID. This process would have produced a higher

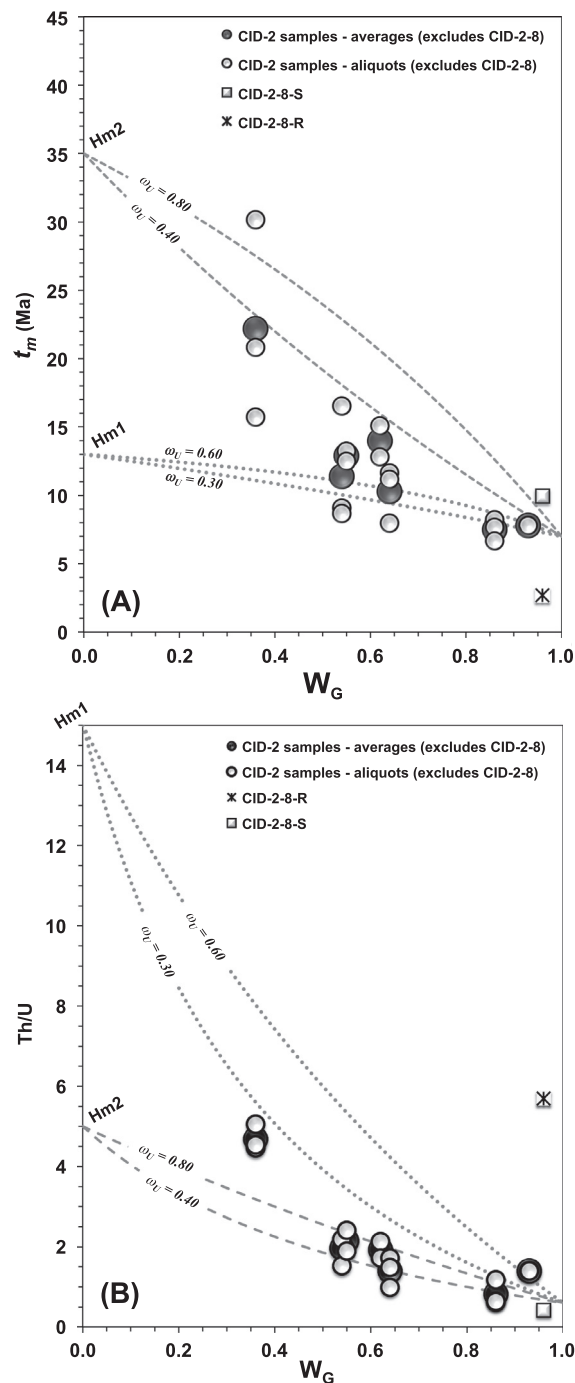


Fig. 6. (A) “Uncorrected” (U-Th)/He ages measured for micro-gram aliquots of the mixtures of minerals in the CID-2 samples of Mesa J (these mixture ages are identified as t_m) are plotted against W_G . (B) Th/U ratios for those same micro-gram aliquots are also plotted against W_G (W_G = the HTNW-compensated mass fraction of goethite in a sample). W_G was measured for powdered, gram-sized samples of CID-2. The dashed and dotted curves were calculated using a mixing model. See text.

Th/U ratio and a corresponding, apparently younger radiometric age in proximate minerals. CID-2-8-R might have been an aliquot that, by happenstance, included such

material in the (U-Th)/He analysis. The aliquot may serve as a cautionary tale about the care needed in sampling.

If something like the preceding scenario produced the “anomalous” result of CID-2-8-R, the type of complication it poses could be avoided by analysis of well-cleaned ultrasonic residue (e.g., Evenson et al., 2014). In fact, another aliquot of the CID-2-8 sample (aliquot CID-2-8-S) has a Th/U ratio of 0.42 and an uncorrected radiometric age of $\sim 10_{(\pm 0.6)}$ Ma. These values are similar to the Th/U ratios and ages of goethite-rich samples CID-2-3 and CID-2-7 (Table 2) and suggest that the “primary” goethite within the ooids of CID-2-8 preserves information on the Miocene environment of Mesa J.

4.3.2. Two-phase mixing – mineral proportions and (U-Th)/He

Averages of the (U-Th)/He ages and Th/U ratios determined for different aliquots of the various CID-2 samples of Table 2 are in Table 4 together with the associated error of the mean (there was only a single age determination for CID-2-7 and thus no error of the mean is reported). Among the CID samples, the average radiometric ages range from ~ 6 Ma to ~ 22 Ma, but there is no monotonic variation of these ages with increasing depth in the core (Table 4). It is remarked again that the average ages in Table 4 have not been adjusted for possible post-crystallization loss of He by diffusion and/or alpha recoil. If the young step ages of the increments of He initially extracted from samples CID-2-3 and CID-2-4 (Fig. 4) indicate some diffusive post-crystallization loss of ^4He and if that loss is representative of all samples, the apparent bulk sample ages in Tables 2 and 4 may underestimate the actual age by $\sim 10\%$.

The (U-Th)/He ages (t_m) from each of the aliquots of the samples of Table 2 are plotted in Fig. 6A against the corresponding values of W_G from Table 4. Similarly, values of the molar ratios of Th/U for each aliquot in Table 2 are plotted against W_G in Fig. 6B. The average ages and Th/U ratios of Table 4 are also plotted against W_G in Fig. 6A and B, respectively. For the three analyzed aliquots of sample CID-2-4 ($W_G = 0.36$), the values of t_m range from 15.7 to 30.2 Ma, whereas the Th/U ratios exhibit a relatively narrow range from ~ 4.5 to 5 (Table 2).

Some of the overall scatter in the data of Fig. 6A and B might be a consequence of the fact that the (U-Th)/He results from all analyzed aliquots of a particular sample are plotted against a single value of W_G for that sample. Grams of powdered, sieved, cleaned, and therefore relatively homogenized, ultrasonic residue of each CID sample were prepared at SMU for “bulk” XRD, XRF, and stable isotope analysis with attendant determinations of bulk values of W_G (Table 4). This contrasts with the microgram-size aliquots that were removed from fragments of the CID-2 samples at the Berkeley Geochronology Center and analyzed for (U-Th)/He ages and Th/U ratios, but not for the abundance of hydrogen—i.e., W_G was not determined for the micro-aliquots. Consequently, small-scale spatial heterogeneities in the proportions of goethite in a CID sample could result in unmeasured, but nevertheless real, variations in W_G among the various microgram aliquots of such a sample. Therefore, pairing the “bulk” values of

W_G in Table 4 with the ages (t_m) and Th/U ratios determined for the micro- aliquots of Table 2 could introduce scatter into the data arrays in Fig. 6A and B. Some scatter might also arise from the presence of the small amounts of quartz in all of the CID-2 samples (Fig. 3), but effects from this source are presumed to be minor.

Notwithstanding the scatter, it is observed that, among the CID-2 samples (exclusive of CID-2-8-R), Th/U and t_m tend to increase with decreasing W_G (Fig. 6A and B). This distribution of data is suggestive of mixtures of younger goethite and older hematite—with higher Th/U in the hematite. Further evidence of such mixtures exists in the ^3He release patterns and step age spectra of CID-2-3 and CID-2-4 (Figs. 4 and 5).

4.3.3. Two-phase mixing—stepwise He release

The diffusivity of He in goethite is generally higher than in hematite, such that higher laboratory temperatures are required to extract He from hematite (e.g., Shuster et al., 2005; Farley and Flowers, 2012; Evenson et al., 2014; Balout et al., 2017). Thus, if stepwise heating analyses are performed on a mixture of these phases, we expect goethite to be the dominant contributor of the He evolved in lower temperature steps, whereas hematite should be the predominant source of He extracted in the later, higher-temperature steps. Furthermore, if there is significant diffusive loss of radiogenic ^4He at Earth-surface temperatures, it is more likely to be from goethite than from hematite (Shuster et al., 2016).

In addition, a solid-state goethite to hematite phase transition commonly occurs at temperatures of ~ 190 °C to 230 °C in vacuum and is monitored by measurement of the evolved structural hydrogen—as H_2O (e.g., Yapp and Poths, 1993; Tabor et al., 2004a, 2004b). The structural changes that accommodate the movement and loss of hydrogen during the phase transition also facilitate the rapid loss of He occluded in the goethite. This is evident in the ^3He release patterns of Fig. 5, which show a rapid increase in the loss of ^3He beginning at ~ 200 °C for both CID-2-3 and CID-2-4—i.e., the goethite to hematite phase change.

The combination of (i) low apparent step ages for the increments of He recovered during the initial heating (Fig. 4), (ii) a subsequent systematic increase to higher step ages, and (iii) a need for temperatures > 200 °C to extract the final $\sim 20\%$ and $\sim 60\%$ of ^3He in, respectively, CID-2-3 and CID-2-4 (Fig. 5) is revealing. This pattern of He release is consistent with lower temperature extraction of He from a younger generation of goethite and higher temperature extraction from older hematite in proportion to the independently determined mass fractions of goethite in these two samples (86% for CID-2-3 and 36% for CID-2-4, Table 4). Moreover, CID-2 samples with higher proportions of hematite exhibit more scatter in the ages of the analyzed aliquots (Fig. 6A), which might indicate the presence of more than one generation of hematite.

4.3.4. Two-phase mixing—radiometric age vs. Th/U

Danišik et al. (2013) measured the amounts of U, Th, and He in CID from a different site on Mesa J to determine

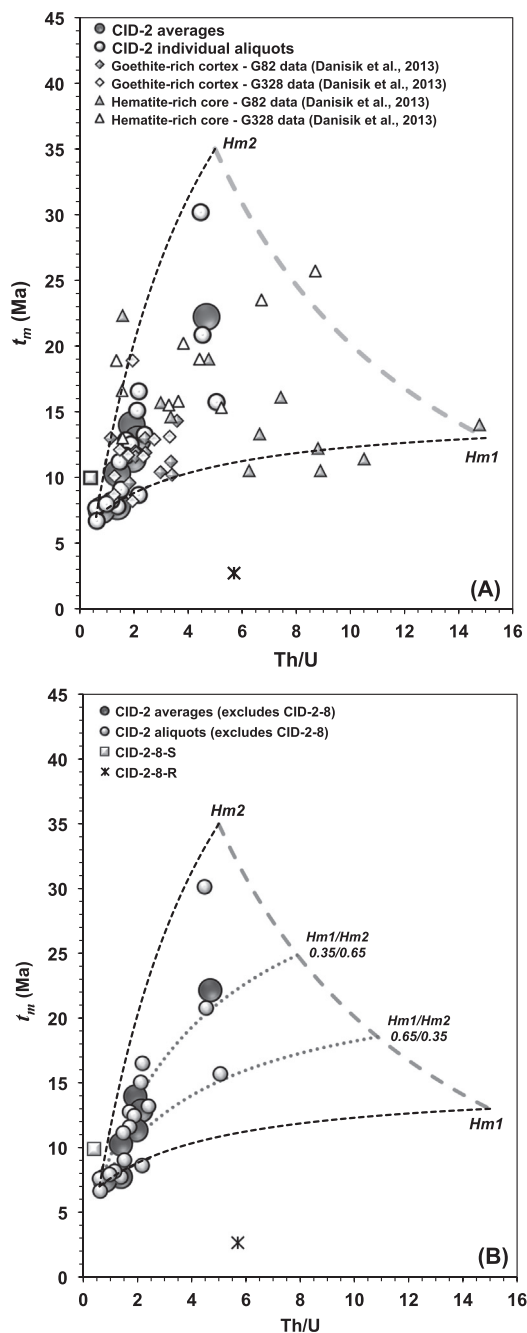


Fig. 7. Plots of t_m against Th/U for CID samples from Mesa J in Western Australia. (A) A plot of the published results of Danišik et al. (2013) for two samples from Mesa J. Their samples were from a different drill core than that which produced the CID-2 samples (see Fig. 1B). For direct comparison, the results for CID-2 from the current work are also shown. (B) Only the results for the CID-2 samples are plotted. The dashed lines represent calculated, two-phase mixing curves that define the boundaries of a three-endmember mixing domain. Mixing of a single generation of goethite with varying proportions of two generations of hematite (Hm1 and Hm2) might explain much of the variation exhibited by the CID-2 data in Fig. 7B. The dotted curves illustrate the effects of variations in the ratio of Hm1 to Hm2 in these mixing scenarios. The two aliquots of CID-2-8 (square and cross) are singled out because of the seemingly anomalous aliquot, CID-2-8-R (cross). See text.

(U-Th)/He ages for paired goethite-rich cortices and hematite-rich cores in ooids of two samples, G82 and G328. As a basis for comparison, those published ages are plotted against the corresponding Th/U ratios in Fig. 7A. Although there is substantial scatter in the data, Danišik et al. (2013) were able to conclude that there were two dominant intervals of hematite crystallization and that, in general, the hematite in the ooids is older than the goethite in those same ooids. Moreover, the molar Th/U ratios of the hematite-rich cores were generally higher than those in the corresponding goethite-rich cortices (Fig. 7A).

The nominal ages and Th/U ratios of the averages and individual aliquots of the CID-2 samples of Tables 2 and 4 are also plotted in Fig. 7A. The CID-2 data array is largely encompassed by the scatter in the data of Danišik et al. (2013). One interpretation of the scatter is that substantial, continuous crystallization of Fe(III) oxides persisted in the Hamersley throughout the Oligocene and Miocene. However, the results in Fig. 6A and B seem to favor an alternative explanation for the samples of Mesa J.

Given that the data of Fig. 6A and B represent evidence for mixing, and with reference to the conclusion of Danišik et al. (2013) that there are two predominant generations of hematite in the ooids of Mesa J, the results of Fig. 7A might be explained by a more episodic crystallization history represented by mixtures of three predominant generations of coexisting Fe(III) oxides—one generation of goethite and two generations of hematite.

4.3.5. Two-phase mixing — model equations

For this discussion, the measured age (t_m) and Th/U data of Fig. 6 are assumed to represent simple mixing of varying proportions of goethite and hematite. The minor amounts of quartz are presumed to play a negligible role. It is assumed that each of the minerals has remained a closed system since the time of its crystallization and that the U and Th decay series are, respectively, in secular equilibrium. It is also assumed for the Cenozoic CID samples of this study that the contributions of ^4He (α particles) from the radioactive decay of the comparatively rare ^{235}U isotope and the very small amounts of ^{147}Sm are negligible and are not considered further (e.g., Wolf et al., 1998).

Therefore, the only significant in situ sources of ^4He in the minerals are presumed to be the successive α -decays in the ^{238}U and ^{232}Th decay series ending with lead:



Then, for radiogenic ^4He :

$$^4\text{He} = [8n_{U_G}\lambda_8 + 6n_{Th_G}\lambda_2]t_G + [8n_{U_H}\lambda_8 + 6n_{Th_H}\lambda_2]t_H \quad (10)$$

λ_2 = decay constant (λ) of $^{232}\text{Th} = 4.9475 \times 10^{-11} \text{ yr}^{-1}$ (Faure, 1986).

λ_8 = decay constant (λ) of $^{238}\text{U} = 1.55125 \times 10^{-10} \text{ yr}^{-1}$ (Faure, 1986).

n_{U_G} = moles of uranium in goethite (G).

n_{Th_G} = moles of thorium in goethite (G).

n_{U_H} = moles of uranium in hematite (H).

n_{ThH} = moles of thorium in hematite (H).
 t_G = the age of the goethite (G) endmember in a mixture.
 t_H = the age of the hematite (H) endmember in a mixture.

Eq. (3) reflects the fact that for U and Th in Cenozoic minerals, $\lambda t \ll 1$, and $e^{\lambda t} \approx 1 + \lambda t$. Thus, with the closed system assumption and an assumption that the minerals contain no ^4He inherited from the local environment at the time of crystallization, the following expression can be derived for the apparent age of a mixture (t_m) of two-phases (goethite and hematite) as determined from (U-Th)/He measurements:

$$t_m = \frac{[8\lambda_8 + 6\sigma_G\lambda_2]W_G t_G + [8\lambda_8 + 6\sigma_H\lambda_2](1 - W_G)\omega_U t_H}{8\lambda_8[W_G + \omega_U(1 - W_G)] + 6\lambda_2[\sigma_G W_G + \sigma_H \omega_U(1 - W_G)]} \quad (11)$$

t_m = the measured (U-Th)/He age of a mixture.

$$\omega_U = n_{U_H} / n_{U_G}$$

$\sigma_G = n_{ThG} / n_{UG}$ = molar ratio of Th to U in the goethite (G) endmember in a mixture.

$\sigma_H = n_{ThH} / n_{UH}$ = molar ratio of Th to U in the hematite (H) endmember in a mixture.

$W_G = m_G^* / m_S^*$ = HTNW-compensated mass fraction of goethite in a sample.

In addition, the atom balance equation for the measured Th/U ratios of the two-phase mixtures is:

$$\frac{Th}{U} = \frac{(\sigma_G - \omega_U \sigma_H)W_G + \omega_U \sigma_H}{(1 - \omega_U)W_G + \omega_U} \quad (12)$$

Th/U = molar ratio of Th to U measured for a mixture.

Other terms are as defined previously. If the respective endmember values of σ_G , σ_H , ω_U , t_G , and t_H are constant among samples with varying mass fractions of goethite (W_G), Eqs. (11) and (12) imply that the measured radiometric age (t_m) of the mixture should be parametrically correlated with the measured molar Th/U ratio. This covariance is exhibited by the CID-2 data array of Fig. 7A. The compared parameters in Fig. 7A were measured in “micro-samples” and thus do not introduce the uncertainty inherent in comparisons of “micro-analyzed” variables (t_m and Th/U) with a “macro-analyzed” variable (W_G) as in Fig. 6A and B.

4.3.6. Two-phase mixing—application of the model

A three-endmember mixing domain would be bounded by two-endmember mixing curves. Calculation of relevant two-endmember mixing curves requires knowledge of the endmember values, t_G , σ_G , t_H , and σ_H , as well as ω_U . The results for goethite-rich CID-2-3 and CID-2-7 in Table 2 suggest an age of ~ 7 Ma and a Th/U ratio of 0.60 as estimates of the values of t_G and σ_G , respectively.

The (U-Th)/He ages and Th/U ratios of the two postulated generations of hematite are less constrained. One of these postulated hematite endmembers (designated Hm1) is assigned a t_{Hm1} value of 13 Ma and a σ_{Hm1} value of 15.

These Hm1 values approximate those reported by Danišik et al. (2013) for an aliquot of a hematite-rich ooid core from their sample G82 (see data point near Hm1 in Fig. 7A).

Vasconcelos et al. (2013) measured (U-Th)/He ages for authigenic goethites and $^{40}\text{Ar}/^{39}\text{Ar}$ ages for authigenic Mn oxides at Lynn Peak in the Hamersley Province that were as old as ~ 31 Ma and ~ 34 Ma, respectively. Those Lynn Peak ages suggest that there was significant dissolution and recrystallization of Fe and Mn oxides in the region at about that time. Therefore, an age of ~ 35 Ma might be an appropriate estimate of the time of crystallization of the Hm2 component in the CID of Mesa J. That age seems especially appropriate, because the results from aliquot CID-2-4-T (Table 2) appear to require the presence of a hematite component of that vintage. A value for σ_{Hm2} is more difficult to constrain but was assumed to be ~ 5.0 . This value is about midway between the extremes of Th/U measured by Danišik et al. (2013) for the three oldest of their hematite-rich ooid cores in Fig. 7A. Thus, $t_{Hm2} = 35$ Ma and $\sigma_{Hm2} = 5.0$.

The calculated mixing curves for the Hm1 and Hm2 endmembers (each paired with the model goethite) are shown in Fig. 7A. Also shown is the corresponding model curve for two-component mixing (gray dashed line) in which the endmembers are the hypothesized hematites, Hm1 and Hm2. To the extent that the CID-2 results of Fig. 6A and B support the idea that it is mixtures of different generations of Fe(III) oxide that produce the scatter in the (U-Th)/He data, the model curves in Fig. 7A illustrate how a three-generation Fe(III) oxide mixing domain might be configured. The values of the model parameters chosen for the hematite endmembers are primarily heuristic, but, although not uniquely constrained, they represent ages and Th/U ratios that are similar to values measured for other Hamersley province Fe(III) oxides/oxyhydroxides.

Without uranium concentration data for model endmembers, ω_U becomes an adjustable parameter. Calculated mixing curves that depict the parametric relationship between t_m and Th/U (Eqs. (11) and (12)) are not sensitive to moderate variations in ω_U . In contrast, shapes of curves depicting t_m (or Th/U) as functions of W_G exhibit substantial sensitivity to ω_U . To illustrate this sensitivity, model goethite-Hm1 curves were calculated for ω_U values of 0.30 and 0.60, whereas goethite-Hm2 curves were calculated for ω_U values of 0.40 and 0.80.

The model curves calculated with those values of ω_U and other previously discussed endmember parameters are plotted in Fig. 6A and B for comparison with the CID-2 data. The model curves bracket most of the data of Fig. 6. This does not affirm that the specified values of ω_U are representative of actual values in the samples. However, the Hm2 curves of Fig. 6A suggest their possible utility by indicating that the mass fraction of goethite (W_G) in micro-aliquot CID-2-4-T (Table 2) might have been 0.15–0.25 instead of the W_G value of 0.36 measured for gram-sized samples of CID-2-4 (Table 4). Future measurements of hydrogen concentrations in the micro-aliquots analyzed for (U-Th)/He could identify local heterogeneities in Gt/Hm ratios and thus test the model.

To reduce clutter and to highlight the relationships between the mixing curves and CID-2 data, Fig. 7B depicts only the data for the CID-2 samples of the current work. One way to illustrate how the mixing curves are changed by changes in the age and Th/U ratio of the Hm2 component is to use the original Hm1 and Hm2 values and simply specify a new hematite endmember that represents a mixture of varying proportions of Hm1 and Hm2. Two such mixing curves (dotted) have been added to Fig. 7B. With this approach, the curve with the hematite endmember labeled “Hm1/Hm2 = 0.35/0.65” accounts for much of the covariance of t_m and Th/U in Fig. 7B. An arbitrarily large number of mixing curves could be calculated from different choices of hematite endmembers. However, the ages chosen for Hm1 and Hm2 of Fig. 7B are consistent with ages published for other CID samples in the Hamersley Province.

The apparent trend of the data of Fig. 7B toward a single goethite endmember (with the outstanding exception of aliquot CID-2-8-R) suggests that much of the goethite in the ooids of Mesa J crystallized at ~ 7 Ma (± 1.0 Ma). Even if there was diffusive loss of as much as $\sim 10\%$ of the radiogenic helium (e.g., Shuster et al., 2005), the corrected age of crystallization of the oolitic goethite would be ~ 7.8 (± 1.0) Ma, which is within the uncertainty of the uncorrected age. This is also similar to the plateau age of ~ 8.4 (± 0.3) Ma determined for goethite-rich CID-2-3 (Fig. 4A), although the nominally older plateau age may represent some contribution of He from the admixed hematite. Therefore, as a working hypothesis, it is assumed that the age of crystallization of the oolitic CID goethite is about 7 (± 1.0) Ma.

Interestingly, an age of ~ 7 (± 1.0) Ma for the goethite in the ooids compares with ages of about 7–9 Ma determined

by Danišik et al. (2013) for the goethite-rich, ferruginized wood fragments in their Mesa J CID samples.

4.4. Hydrogen isotopes in oolitic CID-2 goethites

The δD values of the oolitic CID-2 goethites range from -153‰ to -146‰ (Table 4). This comparatively small range of δD values might be explained by the model-based inference that the oolitic goethites of this study are about the same age, ~ 7 (± 1) Ma, and therefore probably crystallized from isotopically similar late Miocene waters in western Australia.

The histogram in Fig. 8 depicts the δD values of the CID-2 goethites, together with published δD values of natural goethites of various ages from a variety of occurrences (primarily on the continents). If this distribution reflects the hydrogen isotope compositions of ancient meteoric waters, it contains paleoenvironmental information.

4.4.1. δD of meteoric waters – goethite as a proxy

The δD values of hydroxyl minerals are useful proxies of the δD values of the waters present at the time of crystallization if (1) the structural hydroxyl hydrogen in the mineral has remained a closed system and (2) the mineral-water hydrogen isotope fractionation factor ($D\alpha$) is known.

By definition, $D\alpha = (1000 + \delta D_G)/(1000 + \delta D_w)$. Where, $\delta D_G = \delta D$ of the goethite (FeOOH) and $\delta D_w = \delta D$ of the liquid water. Yapp and Pedley (1985) estimated goethite-water hydrogen isotope fractionation factors from natural samples and “high temperature” partial equilibration experiments, whereas Yapp (1987) and Feng and Yapp (2008) determined $D\alpha$ for pure synthetic goethites.

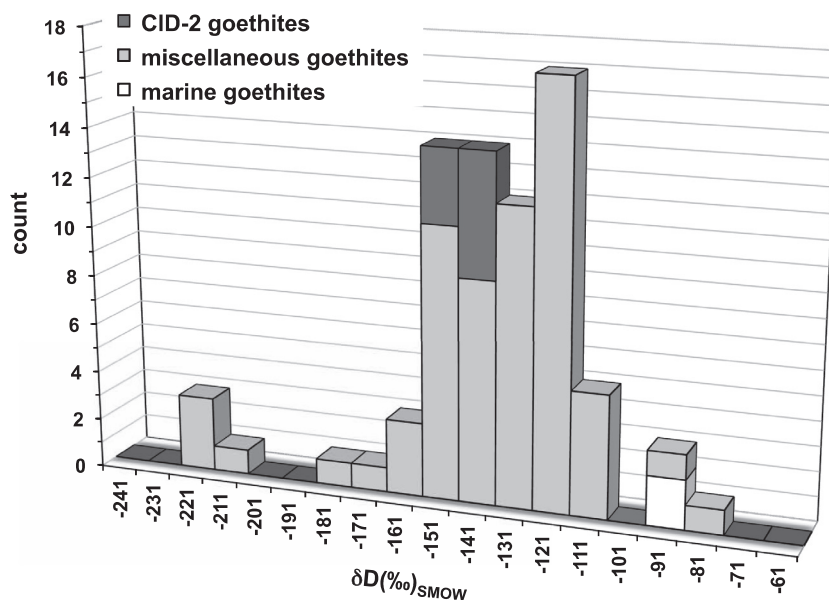


Fig. 8. A histogram of the average Al-adjusted δD values of the CID-2 samples of Table 4. For comparison, the histogram also illustrates the distribution of δD values published for miscellaneous goethites from a wide range of occurrences (sources of published data: Yapp and Pedley, 1985; Yapp, 1987, 2000; Girard et al., 2000; Tabor et al., 2004a, 2004b; Tabor and Yapp, 2005; Hren et al., 2006; Yapp and Shuster, 2011; Gulbranson et al., 2015).

Collectively, these studies found that there was little, or no, variation of D_{α} with temperature for $T < 145$ °C.

The reported values of D_{α} were 0.900_(±0.012) (Yapp and Pedley, 1985), 0.905_(±0.004) (Yapp, 1987), and 0.900_(±0.006) (Feng and Yapp, 2008). These values are analytically indistinguishable and have been of use in the interpretation of the δD values of recent and ancient natural goethites (e.g., Yapp, 1997, 2008; Girard et al., 2000; Tabor et al., 2004a, 2004b; Tabor and Yapp, 2005; Hren et al., 2006; Yapp and Shuster, 2011; Gulbranson et al., 2015). Consequently, we adopt the average (0.902) of these three values as the working value for D_{α} .

For $D_{\alpha} = 0.902$, the inferred δD values of the waters present at the time of crystallization of the CID-2 goethites range from -61 to -53 ‰ with an average of -56 ‰. For GMWL-type precipitation, the average δD value of -56 ‰ implies a corresponding $\delta^{18}\text{O}$ of -8.2 ‰. GMWL = global meteoric water line, where $\delta D = 8\delta^{18}\text{O} + 10$ (Craig, 1961).

4.4.2. Modern Hamersley waters

Dogramaci et al. (2012) measured the δD and $\delta^{18}\text{O}$ values of modern rain, surface waters, and groundwaters in the Hamersley Basin. For the current work, average values of the deuterium excess, “ d ”, were calculated from the isotope data for all of the categories of waters analyzed by Dogramaci et al. (2012), where $d = \delta D - 8\delta^{18}\text{O}$ (e.g., Rozanski et al., 1993). The deuterium excess is a measure of the extent to which a particular sample of water departs from the GMWL of Craig (1961). Values of “ d ” for the modern Hamersley waters of Dogramaci et al. (2012) are plotted against the corresponding average δD values in Fig. 9A. Evaporation of GMWL-type waters tends to increase the δD value of the residual liquid and decrease “ d ” to values $< +10$ (e.g., Craig and Gordon, 1965; Rozanski et al., 1993). For this discussion (allowing for analytical errors), if the deuterium excess of modern Hamersley waters is within the range $6 \leq d \leq 14$, the waters are considered to be GMWL-type.

In four of the seven categories of modern Hamersley waters in Fig. 9A, $d \leq 5$ and the corresponding δD values are shifted to higher (less negative) values. Applying the stated criterion, these are not GMWL-type waters.

For the remaining three categories of modern waters, the deuterium excess is within 4‰ of the GMWL value of +10‰ (Fig. 9A), and they are considered to be GMWL-type waters. These three GMWL-type groups include rainwaters from comparatively infrequent, but intense, storms that deliver more than 20 mm of precipitation per event and two categories of aquifers described as “fractured” and “shallow alluvium” (Dogramaci et al., 2012). The infrequency of the intense modern storms is evident in the 3-year study of Dogramaci et al. (2012)—they sampled only eight such rain events. The range of the average δD values of these GMWL-type Hamersley waters (-57 to -51 ‰) overlaps the range of δD (-61 to -53 ‰) inferred for CID-2 waters (Fig. 9A).

One explanation of this overlap could be the existence of relatively recent and complete hydrogen isotope exchange between structural hydroxyl in the oolitic goethite and

modern GMWL-type waters of the Hamersley Province. If such D/H exchange did occur, it would preclude the use of δD values of CID-2 goethites to recover information about Miocene meteoric waters. However, the (U-Th)/He age indicates that the oolitic goethite has been in the solid-state for at least the last ~ 7 million years, which has isotopic implications that are more evident when other observations are considered.

For example, CID mesas in Western Australia, such as Mesa J, sit above the modern water table (Government of Western Australia, 2016). Therefore, much of the oolitic goethite of Mesa J is in the vadose zone and might commonly be in contact with modern waters that are similar to one or more of the four categories of Hamersley waters that are partially evaporated and non-GMWL ($d \leq 5$). The δD values those non-GMWL waters are substantially more positive than the waters whose δD values are recorded in the CID-2 goethites (Fig. 9A). Evidence for waters that were relatively enriched in ^{18}O (thus, also in D) and were present in Mesa J after the crystallization of the oolitic goethites is found in the oxygen isotope composition of the diagenetic calcite of CID-2-1.

4.4.3. Diagenetic calcite waters

The diagenetic calcite in CID-2-1 (Figs. 2B and 3) occurs in veins and pores. Its actual age and temperature of crystallization are unknown, but its textural relationship to the ooids is evidence that the calcite is younger than the (U-Th)/He-dated oolitic goethite of CID-2-1. Modern MAT at Pannawonica is ~ 27 °C, and as a basis for discussion, a calcite (Cc) crystallization temperature of 25 °C is assumed. At 25 °C, the Cc-water ^{18}O is 1.0288 (Friedman and O’Neil, 1977), for which a calcite $\delta^{18}\text{O}$ of +23.6‰ implies water with a $\delta^{18}\text{O}$ of -5.1 ‰. At higher temperatures, the inferred $\delta^{18}\text{O}$ of the water would be higher (less negative).

The values of the deuterium excess of Fig. 9A are plotted in Fig. 9B against the measured $\delta^{18}\text{O}$ of the modern Hamersley waters (Dogramaci et al., 2012). Also shown in Fig. 9B is the $\delta^{18}\text{O}$ value (-5.1 ‰) of the water inferred to have been present at the time of crystallization of the diagenetic calcite. The $\delta^{18}\text{O}$ of this “calcite water” is more positive than the $\delta^{18}\text{O}$ of the GMWL-type waters of Fig. 9B, but it is within the range of $\delta^{18}\text{O}$ values of non-GMWL Hamersley waters ($d \leq 5$; Fig. 9B). If the more positive $\delta^{18}\text{O}$ of the calcite water reflects some degree of evaporation of the water prior to infiltration into the subsurface (e.g., Dogramaci et al., 2012), it would be indicative of drier conditions than those extant during the crystallization of the oolitic goethites of Mesa J.

The diagenetic calcite $\delta^{18}\text{O}$ result is relevant to the discussion of preservation of hydrogen isotope ratios in ancient goethite. The δD of -147 ‰ measured for the oolitic goethite of sample CID-2-1 indicates a δD of -54 ‰ for the water with which the sample last equilibrated. As seen in a comparison of Fig. 9A and B, the δD of -54 ‰ would not be indicative of the kinds of younger, partially evaporated waters that the diagenetic calcite reveals were present after accumulation of the CID of Mesa J. This lends credence to an assumption that, subsequent to crystallization, the struc-

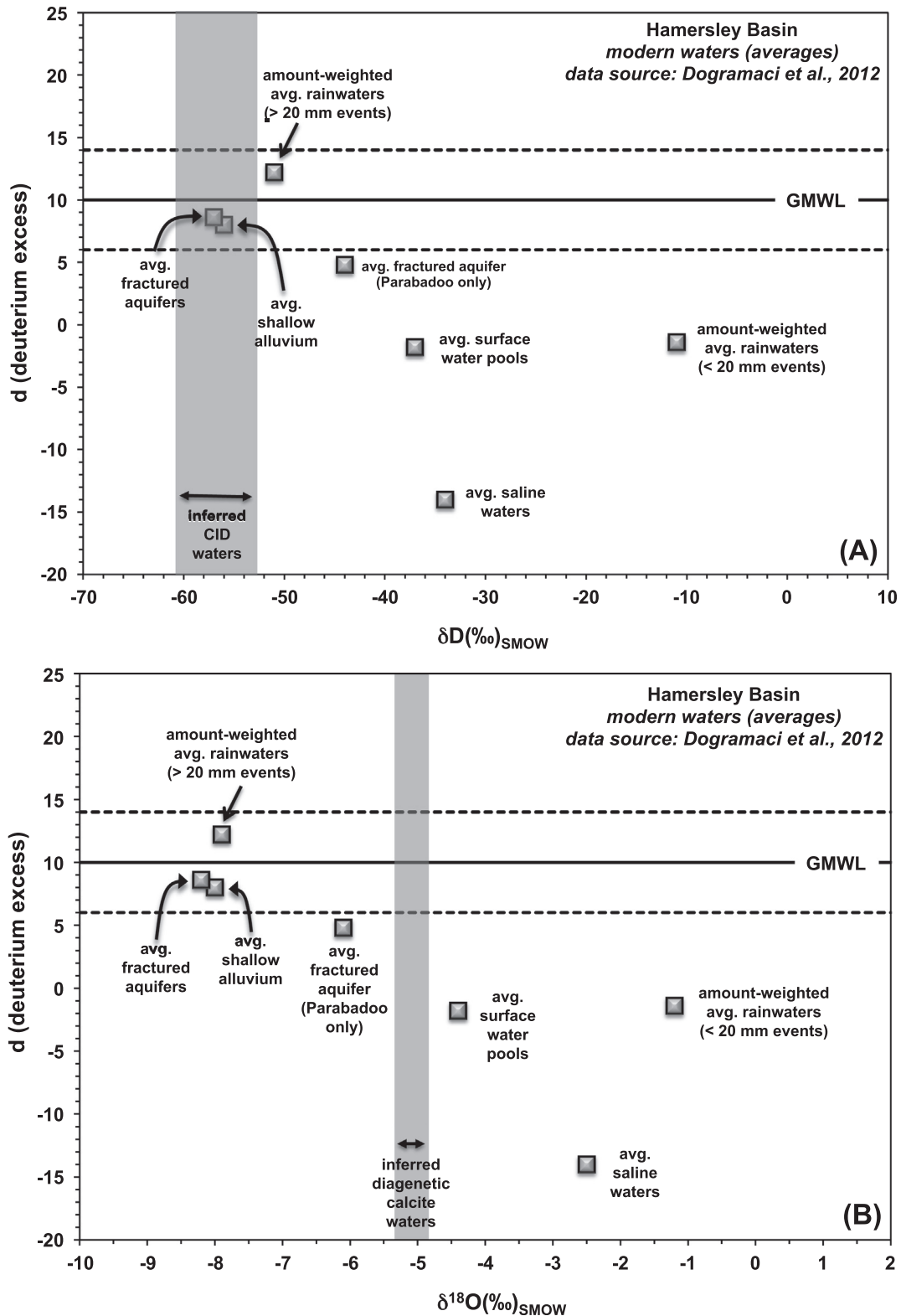


Fig. 9. (A) Values of deuterium excess, “ d ”, ($d = \delta D - 8\delta^{18}\text{O}$) are plotted against the corresponding average δD values of modern waters of the Hamersley Province (reported by Dogramaci et al., 2012). Also shown is the range of δD values of the waters inferred from the δD of CID-2 goethites. The solid horizontal line labeled GMWL represents the deuterium excess of +10 that characterizes the Global Meteoric Water Line (Craig, 1961). The dashed, horizontal lines define an envelope within which values of “ d ” differ from the GMWL value by no more than 4‰. (B) The same modern waters as (A) except that “ d ” is plotted against the $\delta^{18}\text{O}$ values measured by Dogramaci et al. (2012). The $\delta^{18}\text{O}$ value of water inferred from the measured $\delta^{18}\text{O}$ of the diagenetic calcite of CID-2-1 is also shown. See text for discussion.

tural hydroxyl in the oolitic goethite of Mesa J did not exchange hydrogen isotopes with younger waters in the region.

4.4.4. Preservation of ancient D/H ratios in goethite

The uncorrected (U-Th)/He age of ~ 7 Ma deduced for the CID-2 goethites implies that the atoms of radiogenic ^4He (which are not chemically bound) were retained in the goethite crystal structure in sufficiently high proportions on geological time scales to provide seemingly consistent radiometric ages (90% retention or better, Fig. 4A; also, Shuster et al., 2005; Vasconcelos et al., 2013). Thus, the goethite has been an essentially closed system with respect to loss of He since the time of crystallization at about 7 Ma—implying that it did not dissolve and recrystallize

in the intervening interval. This high degree of retention of chemically inert He suggests that hydroxyl hydrogen, which is chemically bound within the goethite structure, could be expected to function as a closed system on that same time scale (at the temperatures of a sedimentary system). Hydrogen isotope data from other natural goethites with constraints on their ages provide some support for this postulate.

Published and new δD values of goethites from a range of environments with ages that were estimated by various methods are listed in Table 6. The difference between the δD of water inferred from goethite ($\delta D_{\text{inferred}}$) and the corresponding δD of ambient modern water (δD_{modern}) is represented as: $\Delta D = \delta D_{\text{inferred}} - \delta D_{\text{modern}}$. Values of $\delta D_{\text{inferred}}$, δD_{modern} , and ΔD are in Table 6, and ΔD is

Table 6
Miscellaneous goethites: ages, δD , inferred water δD , and modern water δD . For calculations of all log t , the units of the estimated age (t) were “years”, not Ma.

Location	Age		dating method	goethite $\delta D(\text{‰})$	inferred ^b modern water		$^{\circ}\Delta D$	source
	Ma	log t			water $\delta D(\text{‰})$	water $\delta D(\text{‰})$		
Atlantis II Deep, Red Sea	0.011	4.04	^{14}C	-93	+6	+8	-2	8
Louisiana Axel Heiberg, Canada	0.3	5.5	(U-Th)/He	-115	-19	-18	-1	1a
Western Australia	7	6.85	(U-Th)/He	{-147 -147}	{-54 -54}	{-57 -11}	{3 -43}	{1b 1b}
Roraima, Brazil	31	7.5	(U-Th)/He	-139	-45	-21	-24	2
Pikes Peak, Colorado	105	8.0	(U-Th)/He	-113	-17	-100	83	2
Ione Fm, California	52	7.7	stratigraphic	-150	-58	-50	-8	7
Neda Fm, Wisconsin	445	8.65	stratigraphic	-139	-45	-60	15	6
Argentina	311	8.49	stratigraphic	-94	4	-30	34	5
Argentina	311	8.49	stratigraphic	-83	17	-30	47	5
French Guiana	> 1	^a 6.3	weathering rate	-121	-25	-16	-9	3
French Guiana	> 1	^a 6.3	weathering rate	-122	-27	-16	-11	3
French Guiana	≤ 1	6.0	weathering rate	-112	-16	-16	0	3

^a An age of 2×10^6 yr was estimated for calculation of log t (Girard et al., 2000).

^b Modern water δD values are from the source indicated in the table, or from Craig (1966), Coplen and Kendall (2000), IAEA/WMO (2006), or Dogramaci et al. (2012).

^c $\Delta D = \delta D_{\text{inferred}} - \delta D_{\text{modern}}$ of waters. Sources: **1a**. This work: goethite δD and average age are newly reported for goethite in sample HLLA-1-1, a ferricrete from an outcrop of weathering rock in the Claibourne Group, Louisiana, USA (collected by CJY). **1b**. This work: CID-2-1. **2**. Goethite δD from Yapp (2000); average age newly reported for this work. **3**. Girard et al. (2000). **4**. Yapp and Shuster (2011). **5**. Gulbranson et al. (2015). **6**. Yapp (1993). **7**. Yapp (2008). **8**. Goethite δD from Yapp (2000); approximate ^{14}C age from Hackett and Bischoff (1973).

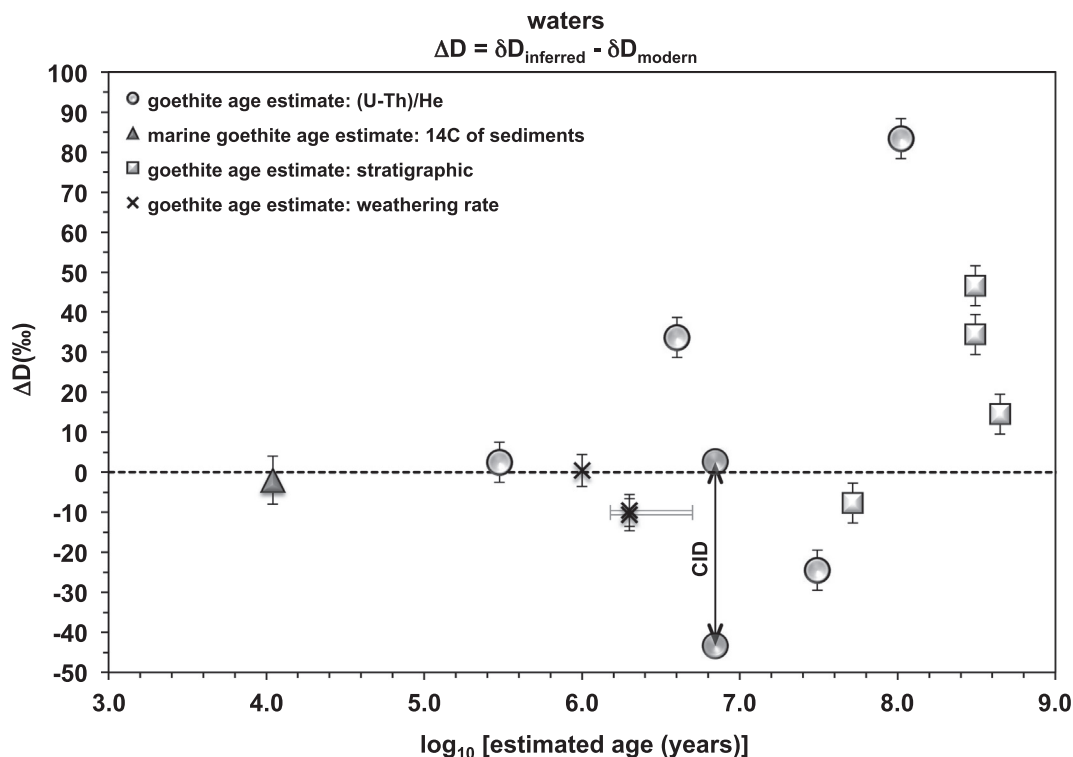


Fig. 10. ΔD values for waters associated with goethites of various ages and locales. $\Delta D = \delta D_{\text{inferred}} - \delta D_{\text{modern}}$. ΔD is plotted against the estimated age of the goethites of Table 6. The (U-Th)/He ages are probably the most robust and are good evidence that those goethites have remained in the solid state over the time represented by their radiometric ages. The scatter in the ΔD values supports an assumption that, in the absence of dissolution/recrystallization, structural hydroxyl hydrogen in goethite preserves information on the δD of the waters present at the time of crystallization. The arrow and data points labeled “CID” reflect the range of δD values of modern Hamersley waters.

plotted against the base 10 logarithm of the age of the goethite in Fig. 10. The ages were estimated by one of four methods: (a) (U-Th)/He dating; (b) stratigraphic context; (c) weathering rate; and (d) ^{14}C -dating of sediments.

Ages that were determined by the radiometric (U-Th)/He method might be the most robust indicators of the actual ages of crystallization and thus of the duration of the interval over which the goethites have remained solids. The oldest of the (U-Th)/He-dated samples of Fig. 10 is from the vicinity of Pikes Peak, Colorado (Table 6). It has an average age of $\sim 10^8$ Ma and a ΔD of 83‰. A value of ΔD of that magnitude indicates that the goethite has not isotopically equilibrated with modern waters.

The Pikes Peak result and the overall scatter in the ΔD data of Fig. 10 support the following assumption: Structural hydroxyl in goethite that persists in the solid state can preserve hydrogen isotope information about a variety of ancient environments, perhaps on time scales of as much as 10^8 years. Therefore, if $\Delta D \approx 0$ ‰ for goethites of reliably known age (i.e., no intervening dissolution and re-precipitation), it would indicate that crystallization occurred at a time in which the δD of ancient waters was similar to the δD of modern waters in that locale.

The possibility of partial, post-crystallization, hydrogen isotope exchange of structural hydroxyl in goethite cannot be ruled out with the existing data. However, as seen in Fig. 10, some of the largest absolute values of ΔD occur

in the oldest samples, which suggests that solid-state preservation of ancient goethite δD values is relatively robust at sedimentary temperatures.

Thus, it is assumed that the measured δD values of the CID-2 goethites preserve information on the D/H ratios of the waters present at the radiometrically-dated time of crystallization. If so, the similarity of the δD values of modern, infrequent, high intensity rainfall in the Hamersley Province to the inferred δD values of late Miocene meteoric waters has interesting paleoenvironmental implications.

4.4.5. Geography and modern meteoric waters

Variations in the D/H and $^{18}\text{O}/^{16}\text{O}$ ratios of rain and snow in the modern hydrologic cycle can be related to variations in air temperature (e.g., Dansgaard, 1964; Friedman et al., 1964; Rozanski et al., 1993; Kohn and Welker, 2005). Latitude and altitude are spatial variables that correlate with temperature. Therefore, the isotope ratios of modern meteoric waters vary systematically with latitude and/or altitude, providing a framework for interpretation of the isotopic compositions of ancient precipitation—including the Late Miocene meteoric waters associated with the crystallization of CID-2 goethites (e.g., Rozanski et al., 1993; Rowley et al., 2001).

For reference, the δD values of modern average annual precipitation from the global database of the International Atomic Energy Agency (IAEA) are plotted against latitude

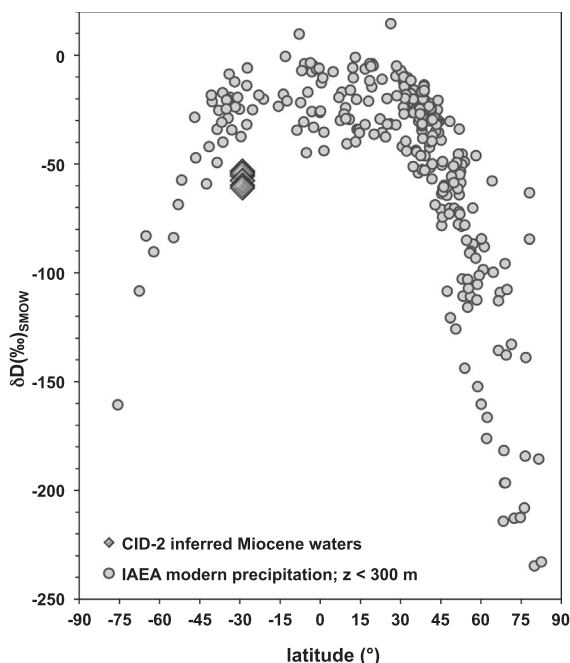


Fig. 11. Average annual δD of modern precipitation plotted against modern latitude (shaded circles) for sites at $z < 300$ m (IAEA/WMO, 2006). z = elevation (sea level datum). The diamond-shaped symbols represent δD values of meteoric waters present at the time (~ 7 Ma) of crystallization of the oolitic CID-2 goethites of Mesa J, which was then at a paleolatitude of $\sim 29^\circ$ S. See text.

in Fig. 11. Southern hemisphere latitudes are shown as negative numbers on the abscissa. To reduce the perturbing effects of the altitude (z) of the local landscape, only those IAEA sites for which $z < 300$ m are included (sea level datum).

4.4.6. Paleo-latitude and ancient meteoric water

From paleomagnetic data, Molina Garza and Fuller (2002) deduced Cenozoic paleolatitudes of selected marine sites in the Great Australian Bight, and thus the rate of northward drift of the Australian continent. For the past 10 Ma, their best-fit rate of drift was 115 mm/yr, which indicates that at ~ 7 Ma the marine sites were at a paleolatitude of $\sim 41^\circ$ S. These marine sites are presently at a latitude of $\sim 34^\circ$ S, whereas Mesa J is currently at $\sim 22^\circ$ S. Therefore, there is a modern latitudinal separation of $\sim 12^\circ$ between Mesa J and the marine sites. If that separation persisted during the latter half of the Neogene, Mesa J would have been at $\sim 29^\circ$ S latitude at ~ 7 Ma.

The δD values of the late Miocene meteoric waters of Mesa J, as inferred from the oolitic CID-2 goethites, are depicted in Fig. 11 at a paleolatitude of 29° S and are more negative than the δD of the modern annual precipitation of the IAEA data set at that latitude. It is possible that this negative shift in the δD of the late Miocene waters reflects comparison with a limited southern hemisphere data set. However, even if the more abundant IAEA data of the northern hemisphere were assumed to represent the scatter that a more complete southern hemisphere data set might

exhibit, there would still be a negative shift in the δD values of the late Miocene meteoric waters of Mesa J relative to the globally distributed modern annual data of Fig. 11.

Monthly δD values of modern precipitation are reported by the IAEA for two coastal sites in the western half of Australia (Darwin and Perth) that, in a latitudinal sense, bracket Mesa J (Fig. 1). Darwin is at $\sim 12^\circ$ S latitude, while Perth is at $\sim 32^\circ$ S. The modern latitude of coastal Perth (32° S) is similar to the inferred Late Miocene paleolatitude ($\sim 29^\circ$ S) of near-coastal Mesa J, which suggests that it may be useful to compare the δD values of the modern Perth and ancient Mesa J precipitation.

The inferred δD values of the late Miocene meteoric waters of Mesa J are represented in the histogram of Fig. 12. Also shown in Fig. 12 is the distribution of the δD values of 39 monthly samples that constitute the population of GMWL-type precipitation in the Perth IAEA dataset (IAEA/WMO, 2006). For this comparison, modern precipitation at Perth was considered to be GMWL-type, if values of the deuterium excess (d) were within the following range: $6 \leq d \leq 14$.

The average δD value of the late Miocene meteoric waters of Mesa J (-56‰) contrasts with the amount-weighted average δD of the modern GMWL-type precipitation at Perth (-17‰). In fact, the inferred δD values of the late Miocene meteoric waters are significantly more negative than even the most negative monthly δD value (-33‰) reported for GMWL-type precipitation at Perth (Fig. 12). This contrast suggests that late Miocene environmental conditions at a paleolatitude of $\sim 30^\circ$ S on the west coast of Australia were substantially different from those of modern Perth.

At ~ 7 Ma, the global climate was cooling from the conditions of the Middle Miocene Climatic Optimum (MMCO), but it was still somewhat warmer in the Late Miocene than at present (Zachos et al., 2001, 2008; Micheels et al., 2007). Yet, those warmer global surface temperatures did not result in more positive δD values for the late Miocene rain in near-coastal, subtropical western Australia. Therefore, other effects are considered.

4.4.7. “Altitude effect”

As used here for surface-collected rainfall, the phrase “altitude effect” refers to observations (and explanatory models) of decreases in δD and $\delta^{18}\text{O}$ of meteoric waters with increases in elevation of the landscape (e.g., Rowley, 2007). If the oolitic CID-2 goethites did not crystallize in paleosols on the ambient flood plain/terraces of the ancient river, but formed instead in weathering environments at higher elevations in the Hamersley province prior to transport and deposition in the channel, an altitude effect might explain at least part of the negative shift in δD values inferred for the Late Miocene meteoric waters. A partial explanation involving an altitude effect might also apply if the CID goethite crystallized in rapidly lithified fluvial sediments (e.g., Morris and Ramanaidou, 2007) in the presence of groundwater (derived from river water) that originally fell as rain in the uplands.

At present, the elevation (z) of much of the surface of the Hamersley uplands is ~ 500 – 600 m (e.g., Vasconcelos

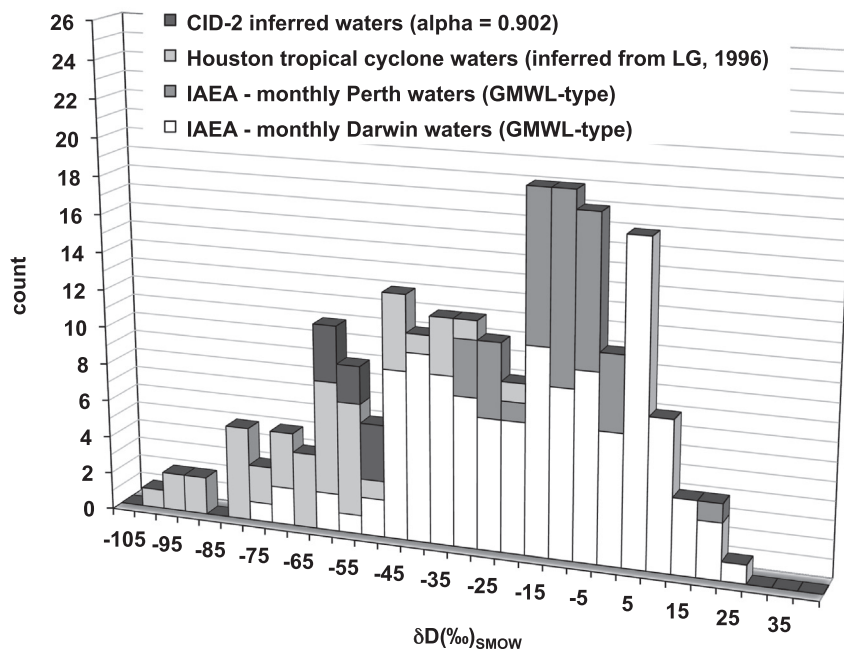


Fig. 12. A histogram of the δD values of late Miocene meteoric waters on Mesa J in Western Australia as inferred from the δD of the oolitic CID-2 goethites. Also, shown in the figure are the distributions of modern monthly GMWL-type rainfall at tropical Darwin and subtropical Perth, Australia (Fig. 1). In addition, the histogram depicts the distribution of δD values of rain from modern tropical cyclones that made landfall near Houston, Texas (the δD data were inferred from the Houston $\delta^{18}\text{O}$ data of Lawrence and Gedzelman, 1996—referenced in the figure as LG, 1996). See text.

et al., 2013; also, Australian Government – Geoscience Australia). Even if the Neogene rates of erosion of about 3.3–3.8 m/Myr estimated for NW Queensland (Vasconcelos and Conroy, 2003) were applicable to western Australia over the past ~ 7 Ma, the overall late Miocene elevation of the uplands of the Hamersley province would not have been much higher than ~ 600 m (sea level datum). For $z \approx 600$ m, a landscape-related altitude effect might have resulted in GMWL-type rainfall with δD values that were ~ 6 – 12‰ more negative than the average δD of precipitation at sea level (e.g., Poage and Chamberlain, 2001; Rowley, 2007). An altitude effect of this magnitude would only account for a small portion of the observed difference of $\sim 40\text{‰}$ between modern, near-sea level precipitation at Perth and Late Miocene precipitation recorded by CID-2 goethites.

4.4.8. Sea level and the volume of continental ice sheets

If the volumes of high latitude continental ice sheets in the late Miocene were smaller than today, sea levels would have been higher and the δD and $\delta^{18}\text{O}$ values of the global oceans would have been somewhat more negative. That, in turn, might have produced a systematic, negative shift in the δD and $\delta^{18}\text{O}$ of meteoric waters.

For an ice-free Earth, sea level would be ~ 100 m higher than at present (e.g., Van Sickle et al., 2004). In that extreme climatic case, addition of low- ^{18}O and low-D melt-water would decrease the $\delta^{18}\text{O}$ of the oceans by about 1‰ (e.g., Savin, 1977), with an accompanying decrease in δD of $\sim 8\text{‰}$ (Yapp, 2000). Global sea level during the Late Miocene (~ 7 Ma) was probably no more than ~ 25 m

higher than today (Van Sickle et al., 2004). If this difference in sea level were due entirely to addition of glacial melt-water, it would represent about 25% of the volume of the modern continental ice sheets on Antarctica and Greenland. Assuming that the late Miocene continental ice sheets had isotopic compositions similar to the modern ice sheets, the δD of the oceans at that time would have been lower by approximately 25% of 8‰ (i.e., $\sim 2\text{‰}$ more negative). A corresponding decrease of only 2‰ in the δD of late Miocene meteoric waters could not explain the shift of about 40‰ inferred from CID-2 goethites.

4.4.9. Storm type

The observation that goethite is commonly a product of wet, oxidizing environments (Schwertmann, 1988) and the fact that there is abundant oolitic goethite in the Late Miocene CID suggest that the weathering systems in which the ooids developed and evolved experienced seasonally contrasting rainfall totaling ~ 1300 – 1700 mm/yr (Tardy et al., 1990). For comparison, modern Perth ($\sim 32^\circ\text{S}$) receives about half that amount of rain (~ 760 mm/yr) with almost 80% of the total falling in the colder months of M-J-J-A-S (World Weather Information Service). As noted, none of the monthly δD values of the modern GMWL-type winter precipitation at Perth are as negative as those determined for the CID-2 waters (Fig. 12). Therefore, at a paleolatitude of $\sim 29^\circ\text{S}$ on the west coast of Australia, storm systems that generated substantial amounts of relatively deuterium-depleted rain appear to have been more frequent and/or intense in the Late Miocene than they are in modern Perth.

Within ~100–150 km of their centers of circulation, tropical cyclones (hurricanes, typhoons) are characterized by often intense and usually copious amounts of rainfall (e.g., Scatena and Larson, 1991; Fudeyasu et al., 2008). Published stable isotope ratios of rain from such storms might be relevant to the interpretation of the inferred δD values of the late Miocene meteoric waters of western Australia.

Fudeyasu et al. (2008) measured hydrogen and oxygen isotope ratios of rain from a western Pacific tropical cyclone (typhoon) that was sampled on a Japanese island (Ishigaki) at a latitude of ~24.5°N and a longitude of ~124.2°E in September of 2006. In general, those paired δD and $\delta^{18}O$ values correspond closely to the GMWL. As estimated from a figure in Fudeyasu et al. (2008), the average δD of the rain in that typhoon was within the range from -70‰ to -60‰ .

Lawrence and Gedzelman (1996) measured and tabulated the $\delta^{18}O$ values of rain from five Gulf of Mexico tropical cyclones that made landfall near subtropical Houston, Texas (~29°N latitude) from 1988 to 1993 in the months from June to September. No precipitation amounts were reported. If the GMWL-like characteristics of the tropical cyclonic rain measured by Fudeyasu et al. (2008) also typified the rain from the tropical cyclones sampled by Lawrence and Gedzelman (1996), the tabulated $\delta^{18}O$ values of the latter imply that the corresponding δD values (Fig. 12) averaged about -65‰ . This average δD of -65‰ contrasts with an inferred δD of -13‰ for “normal” summer rain in Houston (i.e., exclusive of tropical cyclones; Lawrence and Gedzelman, 1996).

Munksgaard et al. (2015) published δD and $\delta^{18}O$ values for rain from a tropical cyclone that made landfall along the northeast coast of Australia (~15–19°S latitude) in April of 2014. The δD values of the majority of the rain samples were within the range from about -100‰ to -40‰ and most of the deuterium excess values (“ d ”) were in the range from 10 to 15. These relatively negative δD values (and GMWL-like values of d) highlight the overall consistency of the isotopic characteristics of rain from tropical cyclones, irrespective of location.

The similarity of the estimated average δD of rain from a western Pacific typhoon (Fudeyasu et al., 2008), five Gulf of Mexico tropical cyclones/hurricanes (Lawrence and Gedzelman, 1996), and an Australian tropical cyclone (Munksgaard et al., 2015) suggests that near-coastal, tropical and subtropical continental sites that are in the paths of such storms could receive substantial amounts of rain with average δD values near -65‰ . Therefore, if a region experienced an increase in the amount of summer-season rain as a consequence of increased frequency and/or intensity of tropical cyclones, the average δD and $\delta^{18}O$ values of the local meteoric water would be expected to become more negative. The isotopic shift could be especially pronounced if the increased summer-season rainfall constituted most of the annual precipitation.

4.4.10. Amount effect

Cullen and Grierson (2007) studied recent climate change as recorded in the oxygen isotope composition of cellulose in tree rings from northwestern Australia. As part

of that work, they noted that monthly precipitation in Darwin during the growing season (N-D-J-F-M) exhibited an overall decrease in $\delta^{18}O$ with increases in the amount of precipitation – i.e., an amount effect in “summer” rain.

That published observation prompted further examination of the Darwin IAEA data for the current work. The histogram in Fig. 12 shows the distribution of δD values for 128 monthly IAEA samples of GMWL-type precipitation from Darwin. Even though Darwin is a tropical site at low elevation (modern latitude ~12°S and $z = 26$ m) with little seasonal variation in monthly average temperatures, the monthly δD of the GMWL-type rain ranges from values as negative as -76‰ up to values as positive as $+24\text{‰}$.

Partial evaporation of GMWL-type waters generally shifts the deuterium excess (d) of the residual liquid to values <10 (e.g., Craig and Gordon, 1965; Rozanski et al., 1993). In an attempt to limit post-condensation evaporation as a factor in any apparent amount effect found in the Darwin IAEA data, but allowing for some analytical uncertainty, our working definition of “GMWL-type” precipitation was further restricted to include only rain samples for which $8 \leq d \leq 14$. With this restriction, the number of GMWL-type IAEA samples at Darwin was 116.

When these monthly data from multiple years were binned in the twelve calendar months of the year, it was found that ten of the calendar months were each represented by at least 4 years of GMWL-type precipitation (Table 7). The under-represented months were June and July. For June, there was only a single year in which the precipitation for that month was GMWL-type; while for July there were no years in which there was GMWL-type precipitation at Darwin. Since no average values of GMWL-type precipitation could be generated for these two months, they are not considered here.

For a particular calendar month, the δD value in Table 7 is a precipitation-weighted average over the years for which that month exhibited GMWL-type rainfall (IAEA/WMO, 2006). Those ten weighted-average, monthly δD values are plotted in Fig. 13 against the corresponding average amounts of monthly precipitation (Table 7). A pattern of decreases in δD values with increases in amounts of rainfall is evident in Fig. 13. This affirms, for GMWL-type rainfall and for a larger percentage of the year at tropical Darwin, the amount effect discussed by Cullen and Grierson (2007).

In coastal and near-coastal northern Australia, the “summer”-half of the year (N-D-J-F-M-A) is the season of monsoonal rains and tropical cyclones (Australian Government Bureau of Meteorology). In tropical Darwin (~12°S latitude), the precipitation that falls in the six “summer” months of N-D-J-F-M-A constitutes, on average, over 90% of the total amount of annual rain (World Weather Information Service), implying that the isotopic composition of, and amount effect for, meteoric water in Darwin is dominated by precipitation delivered by tropical cyclones and/or monsoon-related storms. In addition, the results of Dogramaci et al. (2012) for modern Hamersley Basin rainfall (at ~21°S to 23°S latitude) seem to suggest the presence of an infrequent, tropical cyclone-supported amount effect in that currently dry portion of Western Australia.

Table 7

IAEA data for monthly average amounts and amount-weighted isotopic compositions of GMWL-type precipitation at Darwin, Australia (IAEA/WMO, 2006).

	Average monthly rainfall (mm)	Weighted average $\delta^{18}\text{O}$ (‰) _{SMOW}	Weighted average δD (‰) _{SMOW}	Number of years in that month's average
January	517	-6.1	-38	18
February	321	-6.4	-40	15
March	401	-6.5	-41	19
April	88	-3.8	-19	13
May	40	-2.3	-8	5
August	42	-1.7	-4	4
September	32	-1.9	-6	4
October	85	-1.0	3	12
November	168	-3.3	-14	13
December	254	-4.3	-23	13

For this compilation, a precipitation sample was considered to be GMWL-type if the deuterium excess, “ d ”, was such that $8 \leq d \leq 14$, where $d = \delta D - 8\delta^{18}\text{O}$. June and July are not represented in the table, because there was only a single year in the IAEA data set in which June had GMWL-type precipitation and no years in which that was the case for July. See text.

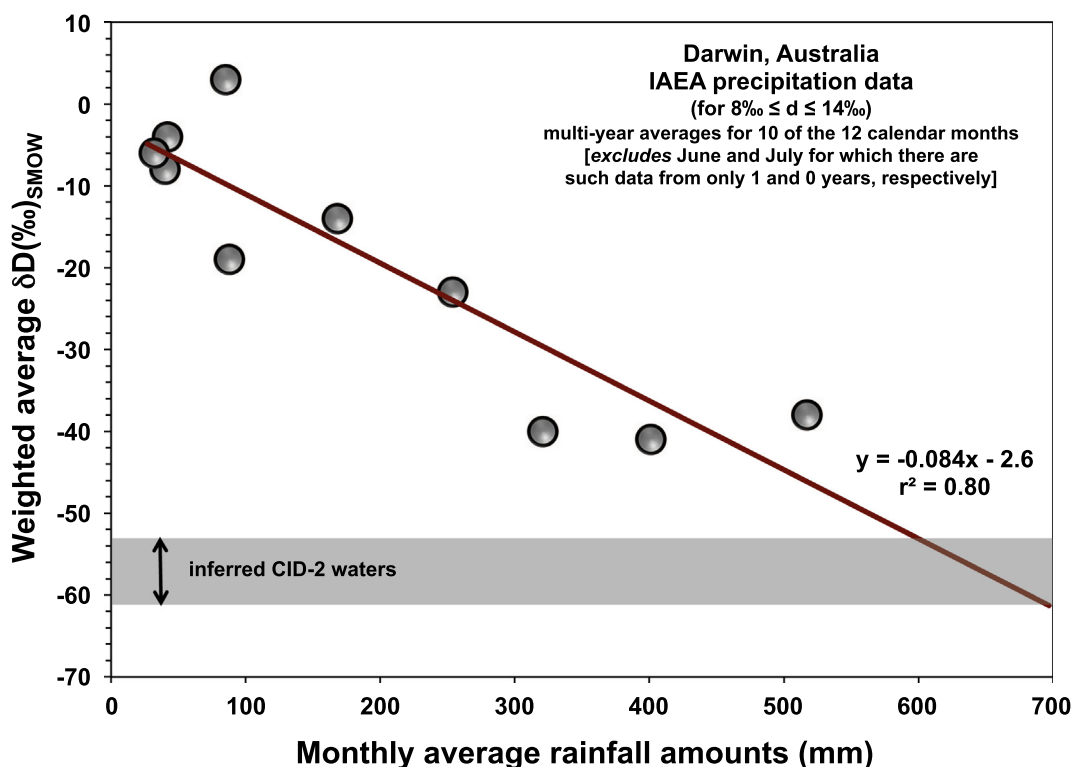


Fig. 13. Monthly average δD values of modern GMWL-type precipitation in tropical Darwin, Australia (IAEA/WMO, 2006). Monthly data from multiple years were binned in the twelve calendar months of the year. Ten of the calendar months were each represented by at least 4 years of GMWL-type precipitation (Table 7). The under-represented months were June and July. They are not considered here. The various δD values in the figure are precipitation-weighted averages (Table 7). An amount effect is exhibited by these GMWL-type data as represented by the linear regression in the figure. The gray band delineates the range of δD values of Late Miocene rain inferred from the δD values of the oolitic CID-2 goethites.

4.4.11. Implications for late Miocene climate

The modern, summer-rain-dominated, monsoonal climate of northern Australia does not extend to the latitude of Perth ($\sim 32^\circ\text{S}$), which as noted, receives most of its rainfall in the winter months (World Weather Information Service). If this latitudinal pattern prevailed in the late Miocene, Mesa J (and environs) would not have received sub-

stantial summer monsoonal rains at its paleolatitude of $\sim 29^\circ\text{S}$.

However, the evidence of the abundant, pedogenic, oolitic CID goethite in those ancient weathering environments seems to require higher rainfall totals with lower average δD values than is currently observed at $\sim 30^\circ\text{S}$ on the west coast of Australia (e.g., Perth). This suggests that either (1)

there were larger amounts of late Miocene winter precipitation with more negative δD values than is the case for winter precipitation in modern Perth or (2) there were increased amounts of relatively low D/H rainfall delivered by more frequent, late Miocene, summer-season tropical cyclones whose storm tracks extended farther south than at present.

If the late Miocene climate was characterized by the first of the foregoing scenarios, the inferred D/H ratios of the ancient meteoric waters of Mesa J imply that the δD values of winter precipitation were ~ 30 – 40% more negative than the δD values of modern winter precipitation at Perth (Fig. 12). Because the global climate of the late Miocene seems to have been somewhat warmer than the modern climate (e.g., Zachos et al., 2001), it is difficult to make a case for that isotopic difference arising from ancient frontal-type winter precipitation with lower D/H ratios than those of modern rain at Perth.

The average δD of -56% inferred for subtropical ($\sim 29^\circ$ S) late Miocene rain in near-coastal western Australia compares with an estimated δD of -65% for rain from modern tropical cyclones in the Gulf of Mexico and the western Pacific. These relatively negative CID-derived δD values seem to support the second scenario: the possibility of an increased frequency/intensity of tropical cyclones at $\sim 29^\circ$ S in the Late Miocene.

Larger amounts of late Miocene summer-season rainfall in near-coastal western Australia at $\sim 30^\circ$ S latitude are not only consistent with the intense chemical weathering that produced the CID (e.g., Tardy et al., 1990), but are also indicated by D-J-F atmosphere-ocean-vegetation simulations for the late Miocene published by Bradshaw et al. (2012). However, Bradshaw et al. (2012) suggested that their results indicating higher amounts of precipitation could be an artifact of the method of performing the simulation.

Higher fluxes of meteoric water from tropical cyclones in the late Miocene summers would have facilitated dissolution and removal of BIF-sourced silica, with relative enrichment in oxidized Fe. Moreover, wetter late Miocene summers would have promoted more biological activity in the aerobic chemical weathering environments, which might have generated multiple cycles of microbially mediated dissolution and recrystallization of Fe(III) oxides (e.g., Hersman et al., 1996, 2001; Grantham et al., 1997; Hsieh and Yapp, 1999). The oolitic textures in the CID may be indicative of such recycling (Dahanayake and Krumbein, 1986).

However, the (U-Th)/He ages indicate that the oolitic goethites analyzed for this study were tantamount to closed systems after ~ 7 Ma. Therefore, in the late Miocene, the environment in the vicinity of Mesa J appears to have changed to conditions that did *not* favor widespread recycling of Fe (III) oxides/hydroxides—perhaps changing from a seasonally wet climate to the modern dry climate.

5. CONCLUSIONS

(U-Th)/He ages were determined for eight samples from a core drilled in an ore-grade channel iron deposit (CID) of the Robe Pisolite of Mesa J in Western Australia. A mixing

model suggests that the age of crystallization of the oolitic goethites in those samples is ~ 7 Ma. Therefore, the goethites have effectively been closed systems for ~ 7 Ma and should preserve a stable hydrogen isotope record of late Miocene rainfall in that locale.

Al-adjusted δD values of the oolitic goethite in the eight samples from Mesa J range from -153% to -146% . The goethite δD values imply that the δD of the late Miocene meteoric waters ranged from -61% to -53% , with an average of -56% . Cenozoic movement of the Australian continent placed Mesa J and environs in the subtropics at a paleolatitude of about 29° S during the late Miocene. Thus, the relatively negative δD values might indicate that near-coastal, late Miocene rain was derived primarily from summer-season tropical cyclones with storm tracks that extended into the subtropics of western Australia. These postulated late Miocene tropical storms would have occurred more often and/or exhibited greater intensity at a paleolatitude of 29° S than is the case for modern sites at $\sim 30^\circ$ S on the west coast of Australia (e.g., Perth). If extrapolations from modern summer season rainfall in tropical Darwin, Australia are useful, the rain that fell during the crystallization of the Mesa J oolitic goethite at ~ 7 Ma might have totaled as much as 600 mm in a month (Fig. 13).

The presence of admixed hematite and quartz complicates determination of the oxygen isotope composition of goethite in the CID. However, if the analytical and conceptual challenges are resolved, $\delta^{18}\text{O}$ data from the CID-2 goethites could further constrain conclusions about the late Miocene subtropical environment. That analytical work is in progress and will be discussed elsewhere.

ACKNOWLEDGMENTS

We thank Dr. Erick R. Ramanaidou of the CSIRO of Western Australia for providing the CID samples from the Mesa J drill core, Dr. Kurt Ferguson for assistance with the mass spectrometric analyses of the hydrogen samples, Ashley (Howe) Justinic for the XRD analyses, and Tyler Fritz for the XRF analyses and measurement of the calcite isotope ratios. The paper benefited from helpful reviews by Dr. Alexis Ault, Dr. Cécile Gautheron, and Dr. Michael Hren. This research was supported by U.S. NSF grant EAR-1250502 to C.J.Y and funding from the Ann and Gordon Getty Foundation to D.L.S.

APPENDIX A. SUPPLEMENTARY MATERIAL

Supplementary data associated with this article can be found, in the online version, at <http://dx.doi.org/10.1016/j.gca.2017.06.036>.

REFERENCES

- Australian Government Bureau of Meteorology. Climate statistics for Australian locations. <http://www.bom.gov.au/climate/averages/tables/cw_005069.shtml>.
- Australian Government – Geoscience Australia. <<http://www.ga.gov.au/scientific-topics/national-location-information/land-forms/elevations#heading-2>>.
- Balout H., Roques J., Gautheron C., Tassan-Got L. and Mbongo-Djimbi D. (2017) Helium diffusion in pure hematite ($\alpha\text{-Fe}_2\text{O}_3$)

- for thermochronometric applications: a theoretical multi-scale study. *Comput. Theoret. Chem.* **1099**, 21–28.
- Bao H. and Koch P. L. (1999) Oxygen isotope fractionation in ferric oxide-water systems: low temperature synthesis. *Geochim. Cosmochim. Acta* **63**, 599–613.
- Bao H., Koch P. L. and Rumble, III, D. R. (1999) Paleocene-Eocene climate variation in western North America: evidence from the $\delta^{18}\text{O}$ of pedogenic hematite. *Geol. Soc. Am. Bull.* **111**, 1405–1415.
- Bao H., Koch P. L. and Thiemens M. H. (2000) Oxygen isotope composition of ferric oxides from recent soil, hydrologic, and marine environments. *Geochim. Cosmochim. Acta* **64**, 2221–2231.
- Bird M. I., Longstaffe F. J., Fyfe W. S. and Bildgen P. (1992) Oxygen isotope systematics in a multi-phase weathering system in Haiti. *Geochim. Cosmochim. Acta* **56**, 2831–2838.
- Bird M. I., Longstaffe F. J., Fyfe W. S., Kronberg B. I. and Kishida A. (1993) An oxygen-isotope study of weathering in the eastern Amazon Basin, Brazil. *Clim. Change Cont. Isotopic Rec. Geophys. Monogr.* **78**, 295–307.
- Boily J. F., Szanyi J. and Felmy A. R. (2006) A combined FTIR and TPD study on the bulk and surface dehydroxylation and decarbonation of synthetic goethite. *Geochim. Cosmochim. Acta* **70**, 3613–3624.
- Bradshaw C. D., Lunt D. J., Flecker R., Salzmann U., Pound M. J., Haywood A. M. and Eronen J. T. (2012) The relative roles of CO_2 and palaeogeography in determining Late Miocene climate: results from a terrestrial model-data comparison. *Clim. Past Discuss.* **8**, 715–786.
- Coplen T.B. and Kendall C. (2000) Stable hydrogen and oxygen isotope ratios for selected sites of the U.S. Geological Survey's NASQAN and benchmark surface-water networks. U.S. Geol. Surv. Open-File Rep. 00–160, 409p.
- Coplen T. B., Kendall C. and Hopple J. (1983) Comparison of stable isotope reference samples. *Nature* **302**, 236–238.
- Cullen L. E. and Grierson P. F. (2007) A stable oxygen, but not carbon, isotope chronology of *Callitris columellaris* reflects recent climate change in north-western Australia. *Climatic Change* **85**, 213–229.
- Craig H. (1961) Isotopic variations in meteoric waters. *Science* **133**, 1702–1703.
- Craig H. and Gordon L. I. (1965) Deuterium and oxygen 18 variations in the ocean and marine atmosphere. In: *Stable Isotopes in Oceanographic Studies and Paleotemperatures*, Proceedings of the Third Spoleto Conference, Tongiorgi E., ed., pp. 1–122.
- Craig H. (1966) Isotopic composition and origin of the Red Sea and Salton Sea geothermal brines. *Science* **154**(3756), 1544–1548.
- Dahanayake K. and Krumbein W. E. (1986) Microbial structures in oolitic iron formations. *Mineral. Deposita* **21**, 85–94.
- Danišik M., Evans N. J., Ramanaidou E. R., McDonald B. J., Mayers C. and McInnes B. I. A. (2013) (U–Th)/He chronology of the Robe River channel iron deposits, Hamersley Province, Western Australia. *Chem. Geol.* **354**, 150–164.
- Dansgaard W. (1964) Stable isotopes in precipitation. *Tellus* **16**, 436–468.
- Deng X. D., Li J. W. and Shuster D. L. (2017) Late Mio-Pliocene chemical weathering of the Yulong porphyry Cu deposit in the eastern Tibetan Plateau constrained by goethite (U–Th)/He dating: Implication for Asian summer monsoon. doi: <http://dx.doi.org/10.1016/j.epsl.2017.04.043>.
- Dogramaci S., Skrzypek G., Dodson W. and Grierson P. F. (2012) Stable isotope and hydrochemical evolution of groundwater in the semi-arid Hamersley Basin of subtropical northwest Australia. *J. Hydrol.* **475**, 281–293.
- EPICA Community Members (2004) Eight glacial cycles from an Antarctic ice core. *Nature* **429**, 623–628.
- Evenson N. S., Reiners P. W., Spencer J. E. and Shuster D. L. (2014) Hematite and Mn oxide (U–Th)/He dates from the Buckskin-Rawhide detachment system, western Arizona: gaining insights into hematite (U–Th)/He systematics. *Am. J. Sci.* **314**, 1373–1435.
- Farley K. A. and Flowers R. M. (2012) (U–Th)/Ne and multidomain (U–Th)/He systematics of a hydrothermal hematite from eastern Grand Canyon. *Earth Plan. Sci. Lett.* **359–360**, 131–140.
- Faure G. (1986) *Principles of Isotope Geology*, second ed. Wiley, New York, p. 589.
- Feng W. and Yapp C. J. (2008) Experimental tests of the effects of Al substitution on the goethite-water D/H fractionation factor. *Geochim. Cosmochim. Acta* **72**, 1295–1311.
- Friedman I. and O'Neil J. R. (1977) Data of geochemistry, sixth edition, Compilation of stable isotope fractionation factors of geochemical interest, Geol. Surv. Prof. Pap. 440-KK.
- Friedman I., Redfield A. C., Schoen B. and Harris J. (1964) The variation of the deuterium content of natural waters in the hydrologic cycle. *Rev. Geophys.* **2**, 177–224.
- Friedrich A. J., Beard B. L., Rosso K. M., Scherer M. M., Spicuzza M. J., Valley J. W. and Johnson C. M. (2015) Low temperature, non-stoichiometric oxygen-isotope exchange coupled to Fe(II)–goethite interactions. *Geochim. Cosmochim. Acta* **160**, 38–54.
- Fudeyasu H., Ichiyanagi K., Sugimoto A., Yoshimura K., Ueta A., Yamanaka M. D. and Ozawa K. (2008) Isotope ratios of precipitation and water vapor observed in Typhoon Shanshan. *J. Geophys. Res.* **113**, D12113. <http://dx.doi.org/10.1029/2007JD009313>.
- Garrels R. M. and Christ C. L. (1965) *Solutions, Minerals, and Equilibria*. Harper and Row, New York, p. 450.
- Girard J. P., Razanadrarosa D. and Freyssinet P. (1997) Laser oxygen isotope analysis of weathering goethite from the lateritic profile of Yaou, French Guiana: paleoweathering and paleoclimatic implications. *Appl. Geochem.* **12**, 163–174.
- Girard J. P., Freyssinet P. and Gilles C. (2000) Unraveling climatic change from intra-profile variation in oxygen and hydrogen isotopic composition of goethite and kaolinite in laterites: an integrated study from Yaou, French Guiana. *Geochim. Cosmochim. Acta* **64**, 4467–4477.
- Girard J.-P., Freyssinet P. and Morillon A.-C. (2002) Oxygen isotope study of Cayenne duricrust paleosurfaces: implications for past climate and laterization processes over French Guiana. *Chem. Geol.* **191**, 329–343.
- Government of Western Australia (2016) Groundwater assessment of the north-west Hamersley Range. Department of Water, *Hydrogeological record series, Report no. HG62* (August, 2016), 31p. <http://www.water.wa.gov.au/_data/assets/pdf_file/0006/8718/HG62_Aug_2016.pdf>.
- Grantham M. C., Dove P. M. and DiChristina T. J. (1997) Microbially catalyzed dissolution of iron and aluminum oxyhydroxide mineral surface coatings. *Geochim. Cosmochim. Acta* **61**, 4467–4477.
- Gulbranson E. L., Montañez I. P., Tabor N. J. and Limarino C. O. (2015) Late Pennsylvanian aridification on the southwestern margin of Gondwana (Paganzo Basin, NW Argentina): a regional expression of a global climate perturbation. *Palaeogeog. Palaeoclim. Palaeoecol.* **417**, 220–235.
- Hackett J. P. and Bischoff J. L. (1973) New data on the stratigraphy, extent, and geologic history of the Red Sea geothermal deposits. *Econ. Geol.* **68**, 553–564.
- Hersman L., Maurice P. and Sposito G. (1996) Iron acquisition from hydrous Fe(III)-oxides by an aerobic *Pseudomonas* sp. *Chem. Geol.* **132**, 25–31.

- Hersman L. E., Forsythe J. H., Ticknor L. O. and Maurice P. A. (2001) Growth of *Pseudomonas mendocina* on Fe(III) (hydr) oxides. *Appl. Environ. Microbiol.* **67**, 4448–4453.
- Hren M. T., Lowe D. R., Tice M. M., Byerly G. and Chamberlain C. P. (2006) Stable isotope and rare earth element evidence for recent ironstone pods within Archean Barberton greenstone belt, South Africa. *Geochim. Cosmochim. Acta* **70**, 1457–1470.
- Hsieh J. C. C. and Yapp C. J. (1999) Stable carbon isotope budget of CO₂ in a wet, modern soil as inferred from Fe(CO₃)OH in pedogenic goethite: possible role of calcite dissolution. *Geochim. Cosmochim. Acta* **63**, 767–783.
- IAEA/WMO (2006) Global Network of Isotopes in Precipitation (GNIP).
- Kohn M. J. and Welker J. M. (2005) On the temperature correlation of δ¹⁸O in modern precipitation. *Earth Plan. Sci. Lett.* **231**, 87–96.
- Lawrence J. R. and Gedzelman S. D. (1996) Low stable isotope ratios of tropical cyclone rains. *Geophys. Res. Lett.* **23**, 527–530.
- Maynard J. B. (1983) *Geochemistry of Sedimentary Ore Deposits*. Springer-Verlag, New York, Heidelberg, Berlin, p. 305.
- McCrea J. M. (1950) On the isotopic chemistry of carbonates and a paleotemperature scale. *J. Chem. Phys.* **18**, 849–857.
- Micheels A., Bruch A. A., Uhl D., Utescher T. and Volker Mosbrugger V. (2007) A Late Miocene climate model simulation with ECHAM4/ML and its quantitative validation with terrestrial proxy data. *Palaeogeog. Palaeoclim. Palaeoecol.* **253**, 251–270.
- Molina Garza R. S. and Fuller M. (2002) Paleolatitudes and magnetostratigraphy for Cenozoic sediments, ODP Leg 182: The Great Australian Bight. *Earth Planets Space* **54**, 399–413.
- Morris R. C. and Ramanaidou E. R. (2007) Genesis of the channel iron deposits (CID) of the Pilbara region, Western Australia. *Australian J. Earth Sci.* **54**, 733–756.
- Munksgaard N. C., Zwart C., Kurita N., Bass A., Nott J. and Bird M. I. (2015) Stable isotope anatomy of tropical cyclone Ita, North-Eastern Australia, April 2014. *PLoS ONE* **10**(3), e0119728. <http://dx.doi.org/10.1371/journal.pone.0119728>.
- Nahon D., Carozzi A. V. and Parron P. (1980) Lateritic weathering as a mechanism for the generation of ferruginous ooids. *J. Sed. Petrol.* **50**, 1287–1298.
- Neck V., Altmaier M., Müller R., Bauer A., Fanghänel Th. and Kim J. I. (2003) Solubility of crystalline thorium. *Radiochim. Acta* **91**, 253–262.
- Pack A., Gutzmer J., Beukes N. J. and Van Niekerk H. S. (2000) Supergene ferromanganese wad deposits derived from Permian Karoo strata along the Late Cretaceous-Mid-Tertiary African land surface, Ryedale, South Africa. *Econ. Geol.* **95**, 203–220.
- Person M., McIntosh J., Bense V. and Remenda V. H. (2007) Pleistocene hydrology of North America: the role of ice sheets in reorganizing groundwater flow systems. *Rev. Geophys.* **45**, 1–28.
- Plummer L. N. (1993) Stable isotope enrichment in paleowaters of the southeast Atlantic Coastal Plain, United States. *Science* **262**, 2016–2020.
- Poage M. A., Sjostrom D. J., Goldberg J., Chamberlain C. P. and Furniss G. (2000) Isotopic evidence for Holocene climate change in the northern Rockies from a goethite-rich ferricrete chronosequence. *Chem. Geol.* **166**, 327–340.
- Poage M. A. and Chamberlain C. P. (2001) Empirical relationships between elevation and the stable isotope composition of precipitation and surface waters: Considerations for studies of paleoelevation change. *Am. J. Sci.* **301**, 1–15.
- Ramanaidou E. R., Morris R. C. and Horwitz R. C. (2003) Channel iron deposits of the Hamersley Province, Western Australia. *Australian J. Earth Sci.* **50**, 669–690.
- Rowley D. B. (2007) Stable isotope-based paleoaltimetry: theory and validation. *Rev. Miner. Geochem.* **66**, 23–52.
- Rowley D. B., Pierrehumbert R. T. and Currie B. S. (2001) A new approach to stable isotope-based paleoaltimetry: implications for paleoaltimetry and paleohypsometry of the High Himalaya since the Late Miocene. *Earth Planet. Sci. Lett.* **188**, 253–268.
- Rozanski K., Araguas-Araguas L. and Gonfiantini R. (1993) Isotopic patterns in modern global precipitation. *Climate Change in Continental Isotopic Records. Geophys. Mon.* **78**, 1–36.
- Savin S. (1977) The history of the Earth's surface temperature during the past 100 million years. *Ann. Rev. Earth Planet. Sci.* **5**, 319–355.
- Scatena F. N. and Larson M. C. (1991) Physical aspects of hurricane hugo in Puerto Rico. *Biotropica* **23**(4), Part A, pp. 317–323.
- Schulze D. G. (1984) The influence of aluminum on iron oxides. VIII. Unit cell dimensions of Al-substituted goethites and estimation of Al from them. *Clays Clay Miner.* **32**, 36–44.
- Schwertmann U. (1988) Occurrence and formation of iron oxides in various pedoenvironments. In *Iron in Soils and Clay Minerals* (eds. J. W. Stucki, B. A. Goodman and U. Schwertmann). Reidel, Dordrecht, pp. 267–308.
- Shuster D. L. and Farley K. A. (2005) ⁴He/³He thermochronometry: theory, practice, and potential complications. *Rev. Miner. Geochem.* **58**, 181–2003.
- Shuster D. L., Farley K. A., Sisterson J. and Burnett D. S. (2004) Quantifying the diffusion kinetics and spatial distributions of radiogenic ⁴He in minerals containing proton-induced ³He. *Earth Planet. Sci. Lett.* **217**, 19–32.
- Shuster D. L., Vasconcelos P. M., Heim J. A. and Farley K. A. (2005) Weathering geochronology by (U-Th)/He dating of goethite. *Geochim. Cosmochim. Acta* **69**, 659–673.
- Shuster D. L., Farley K. A., Vasconcelos P. M., Balco G., Monteiro H. S., Waltenberg K. and Stone J. O. (2012) Cosmogenic ³He in hematite and goethite from Brazilian “canga” duricrust demonstrates the extreme stability of these surfaces. *Earth Planet. Sci. Lett.* **329–330**, 41–50.
- Shuster D., Reiners P., Ault A., Deng X.-D. and Tremblay M. (2016) Constraining time and temperature from ⁴He/³He thermochronometry of polycrystalline Fe- and Mn-oxide. *Goldschmidt Abstracts* **2016**, 2852.
- Seidel M., Pack A., Sharp Z. D. and Seidel E. (2005) The Kakopetros and Ravdoucha iron-oxide deposits, western Crete, Greece: fluid transport and mineralization within a detachment zone. *Econ. Geol.* **100**, 165–174.
- Siehl, A. and J. Thein (1989) Minette-type ironstones. In: *Phanerozoic Ironstones*, Geol. Soc. Spec. Pub. 46, T.P. Young and W.E.G. Taylor, eds., 176.
- Sjostrom D. J., Hren M. T. and Chamberlain C. P. (2004) Oxygen isotope records of goethite from ferricrete deposits indicate regionally varying Holocene climate change in the Rocky Mountain region, U.S.A. *Quat. Res.* **61**, 64–71.
- Tabor N. J. and Yapp C. J. (2005) Juxtaposed Permian and Pleistocene isotopic archives: Surficial environments recorded in calcite and goethite from the Wichita Mountains, Oklahoma. In: *Isotopic and Elemental Tracers of Cenozoic Climate Change* (Mora G. and Surge D, eds.) Geol. Soc. Am. Spec. Pap. 395, pp. 55–70.
- Tabor N. J., Montañez I. P., Zierenberg R. and Currie B. S. (2004a) Mineralogical and geochemical evolution of a basalt-hosted fossil soil (Late Triassic, Ischigualasto Formation, northwest Argentina): potential for paleoenvironmental reconstruction. *Geol. Soc. Am. Bull.* **116**, 1280–1293.
- Tabor N. J., Yapp C. J. and Montañez I. P. (2004b) Goethite, calcite, and organic matter from Permian and Triassic soils:

- carbon isotopes and CO₂ concentrations. *Geochim. Cosmochim. Acta* **68**, 1503–1517.
- Tardy Y., Kobilsek B., Roquin C. and Paguet H. (1990) Influence of Periatlantic climates and paleoclimates on the distribution and mineralogical composition of bauxites and ferricretes. *Chem. Geol.* **84**, 179–182.
- Tremblay M. M., Fox M., Schmidt J. L., Tripathy-Lang A., Wielicki Harrison T. M., Zeitler P. K. and Shuster D. L. (2015) Erosion in southern Tibet shut down at ~10 Ma due to enhanced rock uplift within the Himalaya. *Proc. Nat. Acad. Sci.* **112**, 12030–12035.
- Van Houten F. B. (1982) Ancient soils and ancient climates. In *Climate in Earth History, Studies in Geophysics*. National Academy Press, Washington, D.C, pp. 112–117.
- Van Houten F. B. and Bhattacharyya D. P. (1982) Phanerozoic oolitic ironstones—geologic record and facies model. *Ann. Rev. Earth Planet. Sci.* **10**, 441–457.
- Van Sickle W. A., Kominz M. A., Miller K. G. and Browning J. V. (2004) Late Cretaceous and Cenozoic sea-level estimates: backstripping analysis of borehole data, onshore New Jersey. *Basin Res.* **16**, 451–465.
- Vasconcelos P. M. and Conroy M. (2003) Geochronology of weathering and landscape evolution, Dugald River valley, NW Queensland, Australia. *Geochim. Cosmochim. Acta* **67**, 2913–2930.
- Vasconcelos P. M., Heim J. A., Farley K. A., Monteiro H. and Waltenberg K. (2013) ⁴⁰Ar/³⁹Ar and (U–Th)/He – ⁴He/³He geochronology of landscape evolution and channel iron deposit genesis at Lynn Peak, Western Australia. *Geochim. Cosmochim. Acta* **117**, 283–312.
- Wolf R. W., Farley K. A. and Kass D. (1998) A sensitivity analysis of the apatite (U–Th)/He thermochronometer. *Chem. Geol.* **148**, 105–114.
- World Weather Information Service. <<http://www.worldweather.org/185/m185.htm>>.
- Yapp C. J. (1987) Oxygen and hydrogen isotope variations among goethites (α-FeOOH) and the determination of paleotemperatures. *Geochim. Cosmochim. Acta* **51**, 355–364.
- Yapp C. J. (1990) Oxygen isotopes in iron (III) oxides. I. Mineral-water fractionation factors. *Chem. Geol.* **85**, 329–335.
- Yapp C. J. (1993) The stable isotope geochemistry of low temperature Fe(III) and Al “oxides” with implications for continental paleoclimates. *Clim. Change Cont. Isotopic Rec. Geophys. Monogr.* **78**, 285–294.
- Yapp C. J. (1997) An assessment of isotopic equilibrium in goethites from a bog iron deposit and a lateritic regolith. *Chem. Geol.* **135**, 159–171.
- Yapp C. J. (1998) Paleoenvironmental interpretations of oxygen isotope ratios in oolitic ironstones. *Geochim. Cosmochim. Acta* **62**, 2409–2420.
- Yapp C. J. (2000) Climatic implications of surface domains in arrays of δD and δ¹⁸O from hydroxyl minerals: goethite as an example. *Geochim. Cosmochim. Acta* **64**, 2009–2025.
- Yapp C. J. (2001) Rusty relics of Earth history: iron (III) oxides, isotopes and surficial environments. *Annu. Rev. Earth Planet. Sci.* **29**, 165–199.
- Yapp C. J. (2007) Oxygen isotopes in synthetic goethite and a model for the apparent pH dependence of goethite-water ¹⁸O/¹⁶O fractionation. *Geochim. Cosmochim. Acta* **71**, 1115–1129.
- Yapp C. J. (2008) ¹⁸O/¹⁶O and D/H in goethite from a North American Oxisol of the Early Eocene climatic optimum. *Geochim. Cosmochim. Acta* **72**, 5838–5851.
- Yapp C. J. (2012) Oxygen isotope effects associated with substitution of Al for Fe in synthetic goethite: some experimental evidence and the criterion of oxygen yield. *Geochim. Cosmochim. Acta* **97**, 200–212.
- Yapp C. J. and Pedley M. D. (1985) Stable hydrogen isotopes in iron oxides-II. D/H variations among natural goethites. *Geochim. Cosmochim. Acta* **49**, 487–495.
- Yapp, C. J. and Poths, H. (1991) 13C/12C ratios of the Fe(III) carbonate component in natural goethites. In: *Stable Isotope Geochemistry: A Tribute to Samuel Epstein* (eds. H.P. Taylor Jr., J.R. O’Neil, I.R. Kaplan), *Geochem. Soc. Spec. Publ.* **3**, pp. 257–270.
- Yapp C. J. and Poths H. (1993) The carbon isotope geochemistry of goethite (α-FeOOH) in ironstone of the Upper Ordovician Neda Formation, Wisconsin, USA: implications for early Paleozoic continental environments. *Geochim. Cosmochim. Acta* **57**, 2599–2611.
- Yapp C. J. and Poths H. (1995) Stable hydrogen isotopes in iron oxides: III. Nonstoichiometric hydrogen in goethite. *Geochim. Cosmochim. Acta* **59**, 3405–3412.
- Yapp C. J. and Shuster D. L. (2011) Environmental memory and a possible seasonal bias in the stable isotope composition of (U–Th)/He-dated goethite from the Canadian Arctic. *Geochim. Cosmochim. Acta* **75**, 4194–4215.
- Young T. P. and Taylor W. E. G. (1989) *Phanerozoic Ironstones. Geol. Soc. Spec. Pub.* **46**. The Geological Society, London, p. 251.
- Xu B.-L., Zhou G.-T. and Zheng Y.-F. (2002) An experimental study of oxygen isotope fractionations in goethite-akaganeite-water systems at low temperature. (in Chinese). *Geochimica* **31**, 366–374.
- Zachos J. C., Pagani M., Sloan S., Thomas E. and Billups J. (2001) Trends, rhythms, and aberrations in global climate 65 Ma to Present. *Science* **292**, 686–693.
- Zachos J. C., Dickens G. R. and Zeebe R. E. (2008) An early Cenozoic perspective on greenhouse warming and carbon-cycle dynamics. *Nature* **451**, 279–283.
- Zheng Y.-F. (1998) Oxygen isotope fractionation between hydroxide minerals and water. *Phys. Chem. Mineral.* **25**, 213–221.

Associate editor: Miryam Bar-Matthews